

Ph.D. Thesis

Systematic errors of cosmological gravity test
using redshift space distortion

Takashi Ishikawa

(Supervisor: Tomonori Totani)

January, 2015

Department of Astronomy, Graduate School of Science
Kyoto University

Abstract

In the late of 1990s the accelerated expansion of the universe was discovered through precise measurements of the distances to type-Ia supernovae. To explain this observational fact, it is needed either the existence of dark energy, which works as repulsive force, in the general relativity framework, or otherwise modified gravity theory that predicts weaker gravity on cosmological scales. In such a situation, redshift space distortion (RSD) effects seen in observed galaxy distribution can be used as an observational powerful tool to test gravity theories on cosmological scales, because the strength of RSD effects predicted from different gravity theories differs from each other. Thus, in advance of analysing observed galaxy data, the systematic uncertainties of RSD test must carefully be examined and understood, especially for future surveys with large statistics.

In this thesis, I firstly review the gravitational evolution of the density fluctuations and introduce RSD models in terms of the power spectrum. I will also explain the galaxy (or halo) bias problem here. Then I summarize our research (Ishikawa et al., 2014) of investigating the systematic errors on the measurement of structure growth-rate parameter, $f\sigma_8$, based on N-body simulations.

In the research, we employed various theoretical RSD models for the two-dimensional halo power spectrum in redshift space, and estimated the systematic errors on the measurements induced by non-linear evolution of the power spectrum and by the halo bias with respect to the dark matter distribution. We generated halo catalogues from 40 realisations of N-body simulation with 1024^3 dark matter particles in the box length of $700 h^{-1}\text{Mpc}$ on a side (equivalently, $3.4 \times 10^8 h^{-3}\text{Mpc}^3$ comoving volume). We considered hypothetical redshift surveys at three redshifts, $z=2, 1.35$ and 0.5 , and made various halo catalogues by varying the minimum halo mass threshold in the wide range of $5.0 \times 10^{11} - 2.0 \times 10^{13} h^{-1}\text{M}_\odot$. We found that the systematic error of $f\sigma_8$ is greatly reduced down to ~ 5 per cent level, when a recently proposed analytical formula of RSD that takes into account the higher-order coupling between the density and velocity fields is adopted, with a scale-dependent bias model. Then we discuss the causes of the systematic errors and their dependence on the halo mass, the redshift and the maximum wavenumber up to which we used in the analysis. Some implications of using this RSD model for future surveys are also discussed. In the research we found that if there are only a small number of modes in the power spectrum, it causes a systematic errors on $f\sigma_8$ measurements, but it can be reduced by applying the Wilson-Hilferty approximation to the measured power spectrum in the likelihood calculation.

Contents

Chapter 1	Introduction	1
1.1	Accelerated expansion of the universe	1
1.2	Redshift space distortion	2
1.3	Redshift surveys for RSD measurement	3
1.4	Systematic errors of linear growth rate measurement	4
1.5	Organization of the thesis	5
Chapter 2	Gravitational evolution of large scale structure	6
2.1	Evolution of the universe	6
2.1.1	Cosmological redshift	6
2.1.2	Friedmann equation and density parameters	7
2.2	Evolution equation of density fluctuations	9
2.3	LSS statistics	12
2.3.1	Correlation function and power spectrum	12
	Two point correlation function	12
	Power spectrum	13
2.3.2	Evolution of the power spectrum	13
2.4	2D power spectrum in redshift space	15
2.4.1	Linear formula of RSD	15
2.4.2	Non-linear RSD model	16
2.5	Galaxy/halo bias	17
2.5.1	Galaxy bias problem	17
2.5.2	RSD formulae for halo power spectrum	18
Chapter 3	N-body simulation, mock catalog generation and power spectrum measurements	19
3.1	N-body simulation with <code>Gadget2</code>	19
3.2	Halo identification	20
3.3	Power spectrum measurement	20
3.3.1	2D power spectrum	20
Chapter 4	Analysis and Results	23
4.1	Parameter estimation analysis	23
4.1.1	Fitting model and model parameters	23
4.1.2	MCMC technique	24
4.1.3	Wilson-Hilferty approximation	25
4.2	linear growth parameter measurement results	27
4.2.1	matter power spectrum	27
4.2.2	halo power spectrum	29

iv Contents

	The case of $z = 1.35$ and $M_{\min} = 1.0 \times 10^{12} h^{-1} M_{\odot}$	29
	Dependence on z and M_{\min}	31
4.3	Implications for Future Surveys	37
Chapter 5	Summary and Conclusion	38
Acknowledgement		40

Chapter 1

Introduction

1.1 Accelerated expansion of the universe

In the late 1990s' precise measurements of the distances to Type-Ia supernovae show that our universe is expanding acceleratedly, and the cosmological constant Λ (or a time-varying dark energy term) that works as repulsive force is needed to explain this fact [1, 2, 3, 4]. As is widely known that the dark energy term obeys the equation of state $p = w\rho$ with $w < -1/3$ (in particular, $w = -1$ for the cosmological constant), meanings that it has negative pressure. Where does it come from? How much does it account for in the universe? To reveal the nature of dark energy is one of the most important tasks of modern cosmology.

From the observations of cosmic microwave background (CMB), which is the thermal radiation emitted omnidirectionally in the universe and up till now has been observed precisely by satellites (i.e. *COBE*, *WMAP* and *Planck*), it is confirmed that CMB has a perfect blackbody radiation at an effective temperature of 2.7 K. This strongly supports the standard big bang theory, in which the universe began about 14 thousand million years ago and has been expanding ever since. However this theory suffers from two major problems, namely, the horizon and flatness problems: the universe appears isotropic *beyond* the particle horizon, and initial energy density needs to be fine-tuned so nearly to the critical density. To solve these problems, thereafter, inflation models have been suggested (e.g., [5]). The inflation universe has a period of increasing its size at an astonishing rate and naturally predicts a very nearly flat universe at present. However a flat universe leads to a strange conclusion that the expansion rate of the universe can be well explained with the energy density of about 30% of materials and 70% of dark energy. Planck team reported that, assuming the general relativity framework and a flat universe, baryonic matter, which has gravity and electromagnetic force and one can observe through luminous flux, accounts for only 4.9%, dark matter (DM) with only gravitational interaction for 26.8% and a cosmological constant for 68.3% [6]. On the other hand, many alternative modified gravity theories to explain the observed accelerated expansion have been suggested (e.g., $f(R)$ gravity [7], DGP brane world [8], Galileon [9]) without introducing the dark energy. Which theory is to be selected as the true nature of the universe? It should be distinguished by only performing accurate and precise observation of the universe, e.g., CMB, galaxy clustering, lensing signal. A research field that draws the true picture of the universe based on the observation data is called as *observational cosmology*.

Especially here in this thesis, I focus on the redshift space distortion (RSD) effects seen in the observed galaxy distribution. Because each of modified gravity theories predicts

different structure growth rates, RSD can help us distinguish them.

1.2 Redshift space distortion

Over recent decades a number of redshift surveys to make detailed three-dimensional (3D) maps of the universe have been performed and the universe shows us its inhomogeneous clusterings, e.g., filament structures of galaxies and structure voids, which are called as the large scale structure (LSS). In Fig. 1.1, I illustrate the appearance of LSS using a dark halo catalogue from my simulation. LSS tells us fertile information of the universe including quantities/properties of matter and dark energy. On large scales of $\sim 100 h^{-1}\text{Mpc}$ we can see baryon acoustic oscillation which is the acoustic feature imprinted in the galaxy distribution by acoustic waves of photon-baryon plasma at recombination epoch. It can be used to constrain baryon fraction in the universe and equation of state of dark energy [10]. On the other hand on small scales (a few – $50 h^{-1}\text{Mpc}$), we can find “redshift space distortion (RSD)” as explained below.

In producing 3D galaxy maps, there is an inevitable systematic contamination due to a observing technique: one measures the distance to a galaxy using its redshift that reflects the universal Hubble flow and the peculiar velocity of the galaxy. Thus the galaxy positions are shifted from those in real-space along line-of-sight, therefore from redshift surveys one always get redshift-space distorted galaxy maps. In the linear regime on large scales, galaxies fall toward the centers of galaxy groups with deep potential and this squishes galaxy distribution along line-of-sight, as known as “the Kaiser effect”. Therefore an apparent clustering signal becomes enhanced on these scales. [11] models

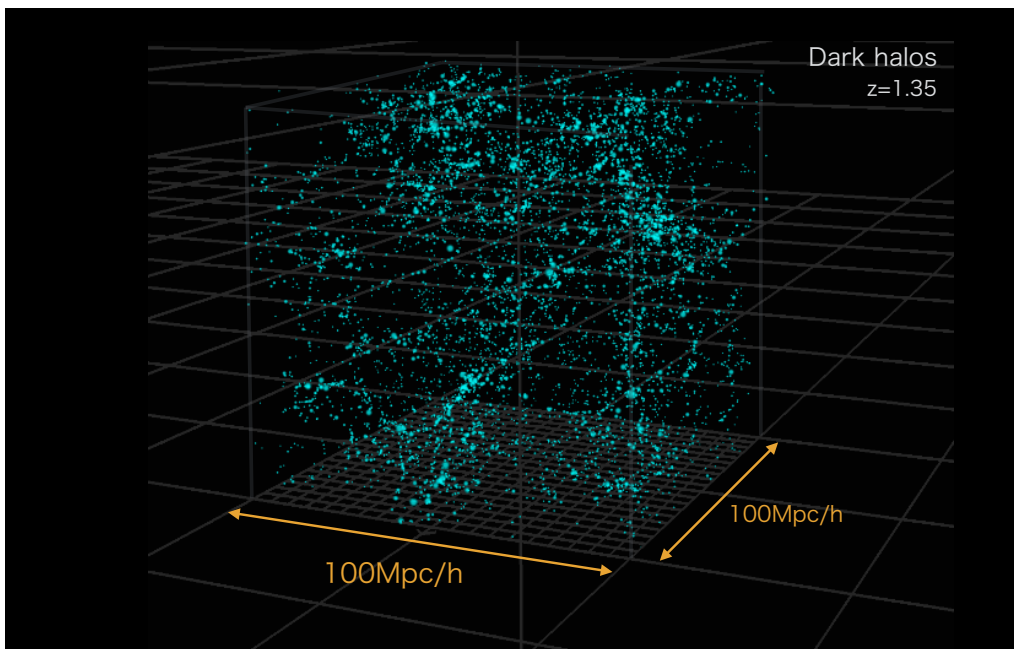


Fig. 1.1. This shows a part of my N-body simulation at redshift $z = 1.35$. Each individual point shows a dark matter halo with radius $\propto M_{\text{halo}}^{1/3}$. There can be seen filamentary dense regions as well as sparse ones.

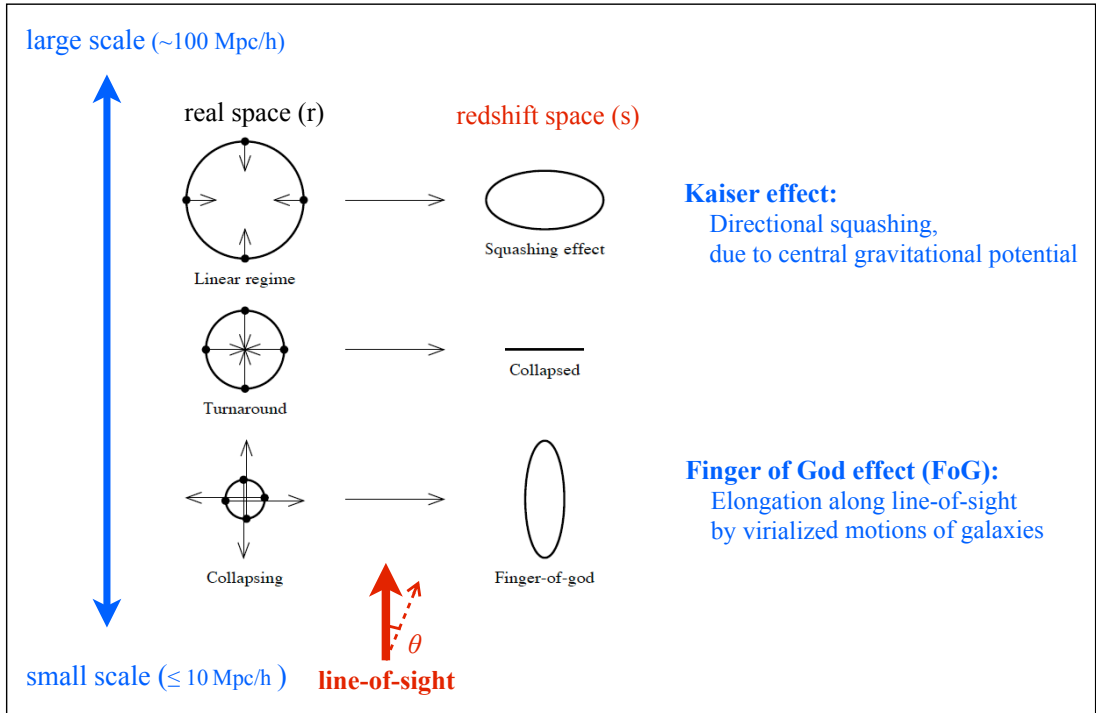


Fig. 1.2. Schematic view of RSD effects. Filled points in left-side column show galaxies in real space and thin arrows on them shows galaxy peculiar velocities. Right-side column shows the images of the observed galaxy distribution in redshift space.

this enhancement in redshift space analytically in terms of the power spectrum, which is one of the most popular statistics in LSS study, with introducing linear growth rate f (please see, sections 2.2 and 2.3). Since the formation history of LSS depends on gravity theories, linear growth rate measurements from redshift surveys give constraints on the gravity theories. For instance, general relativity in a flat Λ CDM universe gives $f = 0.45$ at $z = 0$ in contrast to $f = 1$ for Einstein-de Sitter universe. On the other hand, on small scales where the velocity dispersion of galaxies becomes larger than the coherent infall motions, the clustering signal is smeared out. On such a scale, an elongated feature along line-of-sight arises, which is called as ‘‘Fingers of God (FoG) effect’’ [12, 13]. In Fig. 1.2, I draw a schematic RSD view from [14] with some explanation for the Kaiser and FoG effects.

1.3 Redshift surveys for RSD measurement

A number of measurements of the growth rate have been reported up to $z \sim 0.8$ by using the data from various galaxy surveys (PSCz [15], 2dF [16, 17], 6dF [18] VVDS [19], WiggleZ [20, 21], VIPERS [22], BOSS [23, 24, 25], and SDSS-II[26]). In addition, though the statistical significance is not as large as above, an RSD measurement at even higher redshift $z \sim 3$ is also reported [27].

In the near future we expect more RSD measurements at higher redshifts with larger statistics: Subaru/FastSound project^{*1} ($z \sim 1.3$), which have finished the planned survey

^{*1} <http://www.kusastro.kyoto-u.ac.jp/Fastsound/>

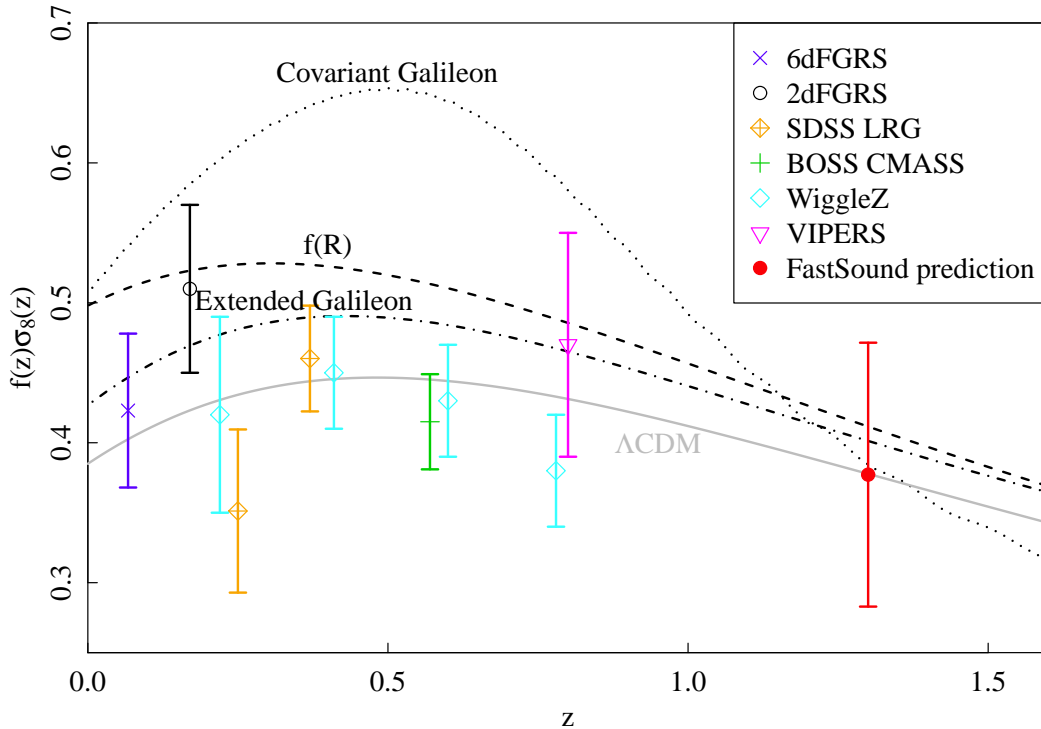


Fig. 1.3. Measured $f\sigma_8$ and their error bars with theoretical predictions from various gravity theories (see labels in the figure). Theoretical curves are calculated assuming $\Omega_{\text{DE}}(\text{or } \Omega_\Lambda) = 0.70$ and $\sigma_8 = 0.811$ cosmology.

and the observed data are under analysis, HETDEX^{*2} ($z \sim 3$), SuMire-PFS^{*3} ($0.7 < z < 1.4$) and space-mission *Euclid*^{*4} ($z > 0.7$), which will cover the whole sky. These observation will give further constraints on modified gravity theories.

In Fig. 1.3 (plotted by okada-san in FastSound team), I show measured $f\sigma_8$ values, which is observable quantity only from galaxy redshift surveys instead of f (see, subsection 2.5.2), from various surveys with some theoretical predictions from gravity theories including Λ CDM universe. (For each modified gravity theory curve, please see [28]). Note that in the figure an expected constraint from FastSound project is also plotted at $z = 1.35$ simply positioned on the Λ CDM curve.

1.4 Systematic errors of linear growth rate measurement

In measuring the linear growth rate there are some effects that could result in systematic errors on it, e.g., the non-linear evolution of the power spectrum and the galaxy bias. These must carefully be examined before survey data analysis, in order to keep the systematic errors smaller than statistical one, especially in advance of future ambitious

*2 <http://hetdex.org/>

*3 <http://sumire.ipmu.jp/>

*4 <http://www.euclid-ec.org/>

surveys.

To estimate the size of systematic error, mock test by using N-body simulation is the most steady way in conceivable, though observed galaxies and dark haloes formed in simulations would not be one-to-one correspondence. There are many investigations in this direction. [29] demonstrated the importance of non-linear corrections in the growth rate parameter measurement by using the multipole moment method for the power spectrum at $z \sim 0.3$. A simple step to go beyond the linear-theory formula is to include the FoG effect on small scales [30, 31, 32, 33, 34]. The presence of any pairwise velocity between galaxies (or even haloes) results in the FoG damping of the clustering amplitude [see, e.g., 35]. This is often phenomenologically modeled by multiplying a damping factor that reflects the pairwise velocity distribution function. In [36], it is found that the RSD parameter $\beta = f/b$ measured by using this approach has a systematic error of up to 10 per cent for galaxy-sized haloes in simulated halo catalogues at $z=1$.

Another step to include the effect of the non-linear evolution is to use analytical redshift-space formulae of the power spectrum and/or the correlation function (the Fourier counter part of the power spectrum) for modestly non-linear scales [35, 37, 38, 39, 40, 41, 42]. [43] shows that an accuracy of 4 per cent is achievable for measurements of f from two-dimensional (2D) two-point correlation functions, when the TNS formula [37] is applied. Note that, in these studies the halo bias was treated as a constant free parameter, or the measured bias from simulation was reincorporated into the model to derive β (or f). However, in real surveys the true bias cannot be measured and hence it is uncertain whether the reported accuracies can really be achieved. In addition to these analytical approaches, there are fully empirical RSD models are suggested based on N-body simulations both in Fourier and in configuration spaces [44, 45, 46].

1.5 Organization of the thesis

In chapter 2, I firstly explain evolutions of the density fluctuations in the universe and introduce the power spectrum as a LSS statistic. Then I derive the RSD formula for 2D power spectrum in linear theory, and also review the non-linear models. Chapter 3 describes N-body simulation, halo catalogue generation and the power spectrum measurements for them. Fitting method and analysis results are presented in chapter 4. In this chapter I will explain the Markov-chain-Monte-Carlo (MCMC) technique with which I measured linear growth parameter $f\sigma_8$ and the other parameters. Chapter 5 is voted to summary of the thesis.

Throughout the thesis, I assume a flat Λ CDM cosmology with the matter density $\Omega_m = 0.272$, the baryon density $\Omega_b = 0.046$, the cosmological constant $\Omega_\Lambda = 0.728$, the spectral index of the primordial fluctuation spectrum $n_s = 0.97$, the amplitude of the density fluctuation $\sigma_8 = 0.81$ and the Hubble parameter $h = 0.70$, which are consistent with the 7-year WMAP results [47].

This thesis is partly supported by collaborators. Dr. Nishimichi provide the code of subhalo finder `subfind` in chapter 3. In chapter 4, I used an improved version of the power spectrum fitting code incorporated with MCMC routine, which was originally developed by him and I used the power spectrum templates provided by Assoc. Prof. Taruya. The other works were created by the author itself.

Chapter 2

Gravitational evolution of large scale structure

In this chapter, I review the evolution of the universe and of the density fluctuation in it. Then I will explain the power spectrum as a statistic for LSS and introduce some RSD models for the 2D halo power spectrum.

2.1 Evolution of the universe

2.1.1 Cosmological redshift

Assuming that the universe is homogeneous, the metric of such a universe can be written as

$$ds^2 = -c^2 dt^2 + a(t)^2 \gamma_{ij} dx^i dx^j \quad (2.1)$$

where ds^2 is a four dimensional distance interval in space-time, c the speed of light, a the scale factor of the universe and γ_{ij} the metric for homogeneous isotropic in 3D space. In the polar coordinates system with (r, θ, ϕ) , by taking radial coordinate r as a sphere of radius r to have surface area of $4\pi r^2$, an interval on the surface becomes

$$d\varphi^2 = d\theta^2 + \sin^2 \theta d\phi^2 \quad (2.2)$$

and then eq. (2.1) is written as

$$ds^2 = -c^2 dt^2 + a(t)^2 \left[\frac{dr^2}{1 - Kr^2} + r^2 (d\theta^2 + \sin^2 \theta d\phi^2) \right] \quad (2.3)$$

(Robertson-Walker metric) where K is the curvature of the space. When we define a new geodesic distance along radial direction at present as

$$dx^2 = \frac{dr^2}{1 - Kr^2} \quad (2.4)$$

and its integral as $r = S_K(x)$, radial coordinate r can be expressed as following forms

$$S_K(x) = \begin{cases} \frac{\sinh(\sqrt{-K}x)}{\sqrt{-K}} & (K < 0, \text{ closed}) \\ x & (K = 0, \text{ flat}) \\ \frac{\sin(\sqrt{K}x)}{\sqrt{K}} & (K > 0, \text{ open}) \end{cases}. \quad (2.5)$$

With this notation, we can rewrite eq. (2.3) with x as

$$ds^2 = -c^2 dt^2 + a(t)^2 [dx^2 + S_K^2(x)(d\theta^2 + \sin^2\theta d\phi^2)]. \quad (2.6)$$

Note that in this metric, the physical distance from origin to a coordinate x at time t becomes $a(t)x$ when we set the scale factor $a = 1$ at present. This coordinate x is referred to as comoving distance.

Then let me explain cosmological redshift z , which is induced by the cosmological expansion, in terms of the scale factor a . Let's think a situation that an observer at the origin observes light at t_0 , which was emitted from x_1 at t_1 . Since light travels along null geodesics with $ds = 0$,

$$cdt = -a(t)dx \quad \text{and} \quad x_1 = \int_{t_1}^{t_0} \frac{cdt}{a(t)} \quad (2.7)$$

hold. The minus sign in the first equation means that light travels in the negative direction. For simplicity one wavelength light is emitted over $(t_1, t_1 + \delta t_1)$ and observed over $(t_0, t_0 + \delta t_0)$, we get

$$\frac{\delta t_1}{a(t_1)} = \frac{\delta t_0}{a(t_0)}. \quad (2.8)$$

Since wavelength at emitted and observed points are $\lambda_s = c\delta t_1$ and $\lambda_o = c\delta t_0$, respectively, the redshift defined as $z = (\lambda_o - \lambda_s)/\lambda_s$ can be expressed as

$$z = \frac{\delta t_0 - \delta t_1}{\delta t_1} = \frac{a(t_0) - a(t_1)}{a(t_1)}. \quad (2.9)$$

By taking t_0 at present and rewrite t_1 as t , we get a simple relation between cosmological redshift and the scale factor as $a(t) = 1/(1+z)$ and comoving distance x becomes

$$x = \int_t^{t_0} \frac{cdt}{a(t)} = \int_a^1 \frac{cda}{a^2 H} = \int_0^z \frac{cdz}{H} \quad (2.10)$$

where $H = \dot{a}/a$ is referred to as the Hubble parameter, which is the expansion rate of the universe and $(\dot{\quad}) = d/dt$.

2.1.2 Friedmann equation and density parameters

The Einstein equation has the form of

$$G_{\mu\nu} = \frac{8\pi G}{c^4} T_{\mu\nu} \quad (2.11)$$

where l.h.s. shows the curvature of the time-space, G the gravity constant and $T_{\mu\nu}$ the Energy-momentum tensor. In the homogenous isotropic universe, this equation can be reduced to following equations:

$$\left(\frac{\dot{a}}{a}\right)^2 = \frac{8\pi G}{3c^2}\rho - \frac{c^2 K}{a^2} \quad (2.12)$$

$$\frac{\ddot{a}}{a} = -\frac{4\pi G}{3c^2}(\rho + 3p) \quad (2.13)$$

and eliminating \ddot{a} by combining these equations we can get the energy-momentum conservation equation as

$$\dot{\rho} + 3\frac{\dot{a}}{a}(\rho + 3p) = 0. \quad (2.14)$$

Here, eq. (2.12) is called as Friedmann equation.

When the universe is filled with well-known component of matter and radiation, eq. (2.13) leads $\ddot{a} < 0$. Einstein believed that the universe was static and to achieve such solution he added cosmological constant Λ as follows

$$G_{\mu\nu} + \Lambda g_{\mu\nu} = \frac{8\pi G}{c^4}T_{\mu\nu}. \quad (2.15)$$

In this case, eqs. (2.12) and (2.13) become

$$\left(\frac{\dot{a}}{a}\right)^2 = \frac{8\pi G}{3c^2}\rho - \frac{c^2 K}{a^2} + \frac{c^2 \Lambda}{3} \quad (2.16)$$

$$\frac{\ddot{a}}{a} = -\frac{4\pi G}{3c^2}(\rho + 3p) + \frac{c^2 \Lambda}{3} \quad (2.17)$$

and setting l.h.s.s of them to be 0, we get static solution as

$$\Lambda = \frac{4\pi G}{c^4}(\rho + 3p), \quad K = \frac{4\pi G}{c^4}(\rho + p). \quad (2.18)$$

Originally the Einstein's constant is a correction term for space curvature, but we can think it to be a kind of energy term in r.h.s.. Then Λ as a energy term has following properties:

$$\rho_\Lambda = \frac{c^4 \Lambda}{8\pi G}, \quad p_\Lambda = -\frac{c^4 \Lambda}{8\pi G}. \quad (2.19)$$

Let's think relation between energy density and pressure by using equation of state $p = w\rho$. Radiation energy density follows $\rho \propto a^{-4}$ and then it gives $w = 1/3$ from eq. (2.14). As the same manner, matter density with $\rho = a^{-3}$ and gives $w = 0$, and cosmological constant gives $w = -1$. In general, an energy term with $\rho + 3p < 0$ (equivalently $w \leq -1/3$) can work as repulsive force and it is called as "dark energy".

Let's think a cosmological model of the flat matter-only universe (known as Einstein-de Sitter universe). In this universe, eq. (2.16) leads the energy density of

$$\rho = \frac{3c^2 H^2}{8\pi G} \quad (2.20)$$

and this is called critical density ρ_{crit} . The universe with total energy density over ρ_c is open whereas it under ρ_c is closed. Density parameter is the fraction of an energy component compared to ρ_{crit} , e.g., $\Omega_{\text{m}} = \rho_{\text{m}}/\rho_{\text{crit}}$ for matter and $\Omega_{\text{r}} = \rho_{\text{r}}/\rho_{\text{crit}}$ for radiation. In addition, following definitions for curvature and cosmological constant are useful as

$$\Omega_{\text{K}} = -\frac{c^2 K}{a^2 H^2}, \quad \Omega_{\Lambda} = \frac{c^2 \Lambda}{3H^2}. \quad (2.21)$$

By using these density parameters, Friedmann eq. (2.16) is represented as

$$1 = \Omega_{\text{r}} + \Omega_{\text{m}} + \Omega_{\text{K}} + \Omega_{\Lambda}. \quad (2.22)$$

Note that $\Omega_{\text{K}} < 0$ (equivalently, $\Omega_{\text{tot}} = \Omega_{\text{r}} + \Omega_{\text{m}} + \Omega_{\Lambda} > 1$) shows a closed universe, whereas $\Omega_{\text{K}} > 0$ ($\Omega_{\text{tot}} < 1$) open universe. The time dependence of the Hubble parameter becomes

$$H^2 = H_0^2 \left(\frac{\Omega_{\text{r}0}}{a^4} + \frac{\Omega_{\text{m}0}}{a^3} - \frac{\Omega_{\text{K}0}}{a^2} + \Omega_{\Lambda 0} \right) \quad (2.23)$$

where subscript 0 means values at present.

Then we can describe the time evolution of the size of the universe as follows: In radiation dominant era, eq. (2.23) is reduced to

$$H^2 = H_0^2 \frac{\Omega_{\text{r}0}}{a^4}, \quad (2.24)$$

leading $a \propto t^{1/2}$. In the same manner, we can get $a \propto t^{2/3}$ for matter dominant era and $a \propto \exp [H_0 \sqrt{\Omega_{\Lambda 0}} t]$ for cosmological constant dominant era.

2.2 Evolution equation of density fluctuations

Galaxy surveys reveal the existence of LSS in the universe and it is naive that LSS is formed by its self-gravity. Therefore to describe the evolution of the density fluctuations is fundamental for understanding LSS correctly and constructing the models of RSD.

The density field should obey following three fundamental equations of fluid motion:

$$\frac{\partial \rho}{\partial t} + \nabla \cdot \rho \mathbf{v} = 0 \quad : \text{continuity} \quad (2.25)$$

$$\frac{\partial \mathbf{v}}{\partial t} + (\mathbf{v} \cdot \nabla) \mathbf{v} = -\nabla \phi - \frac{\nabla p}{\rho} \quad : \text{Euler} \quad (2.26)$$

$$\nabla^2 \phi = 4\pi G \rho \quad : \text{Poisson} \quad (2.27)$$

where ϕ gravity potential (see also [33]). Let me rewrite them in comoving coordinate as $\mathbf{x} = \mathbf{r}/a$ where \mathbf{r} represents the coordinates in physical system. Then comoving velocity \mathbf{u} becomes

$$\mathbf{u} = \dot{\mathbf{x}} = \frac{\mathbf{v}}{a} - \frac{\dot{a}}{a^2} \mathbf{r}, \quad (2.28)$$

here $a\mathbf{u} = \mathbf{v} - H\mathbf{r}$ is called as peculiar velocity. Next, partial derivatives comoving coordinates become

$$\nabla_{\mathbf{r}} = \frac{1}{a} \nabla_{\mathbf{x}} \quad (2.29)$$

$$\left(\frac{\partial}{\partial t} \right)_{\mathbf{r}} = \left(\frac{\partial}{\partial t} \right)_{\mathbf{x}} - H\mathbf{x} \cdot \nabla_{\mathbf{x}}. \quad (2.30)$$

Then, eqs. (2.25) and (2.26) are represented as

$$\frac{\partial \rho}{\partial t} + 3H\rho + \rho \nabla \cdot \mathbf{u} = 0 \quad (2.31)$$

$$\frac{\partial \mathbf{u}}{\partial t} + H(\mathbf{u} \cdot \nabla) \mathbf{u} + (\mathbf{u} \cdot \nabla) \mathbf{u} = -\frac{1}{a^2} \nabla \Phi - \frac{\nabla p}{a^2 \rho} \quad (2.32)$$

where $\Phi = \phi + a\ddot{a}\mathbf{x}^2/2$ is the potential in comoving coordinates, which corresponds that a stationary object in comoving coordinate system is observed as moving acceleratedly in physical one except the origin.

Considering the first order of density perturbation against the homogeneous background density as $\rho = \rho_0 + \delta\rho$ and so on, we can reduce eqs. (2.31) and (2.32) into

$$\frac{\partial \delta}{\partial t} + \nabla \cdot (1 + \delta) \mathbf{u} = 0 \quad (2.33)$$

$$\frac{\partial \mathbf{u}}{\partial t} + 2H\mathbf{u} - \frac{1}{a^2} \nabla \Phi - \frac{\nabla(\delta p)}{a^2 \rho_0} = 0 \quad (2.34)$$

where $\delta(\mathbf{x}) = \delta\rho/\rho_0$, and eq. (2.27) in comoving coordinates is

$$\nabla^2 \Phi = 4\pi G(\rho - \rho_0) = 4\pi G\rho_0 \delta. \quad (2.35)$$

Eliminating \mathbf{u} and Φ by combining these equations, we get the evolution equation of the density fluctuation in comoving coordinates:

$$\frac{\partial^2 \delta}{\partial t^2} + 2H \frac{\partial \delta}{\partial t} - 4\pi G\rho_0 \delta + \frac{\nabla^2(\delta p)}{a^2 \rho_0} = 0. \quad (2.36)$$

By using the relation of the pressure fluctuation δp with the sound speed as $\delta p = c_s^2 \rho_0 \delta$ and performing Fourier transform on the resulting equation, evolution equation in Fourier space becomes

$$\frac{\partial^2 \tilde{\delta}}{\partial t^2} + 2H \frac{\partial \tilde{\delta}}{\partial t} - \left(4\pi G\rho_0 - \frac{c_s^2 k^2}{a^2} \right) \tilde{\delta} = 0 \quad (2.37)$$

where k is the wavenumber. It is worthy to note that, the first term in this equation shows acceleration of the density fluctuation, the second works as resistance term to it due to the cosmic expansion and the third shows the effective gravitational force. Therefore when $4\pi G\rho_0 - c_s^2 k^2/a^2 > 0$, the fluctuation will grow and otherwise it decays. Here the critical wavenumber $k_J = a\sqrt{4\pi G\rho_0}/c_s$, which is referred as Jeans wavenumber, or the corresponding Jeans length as $\lambda_J = 2\pi a/k_J = c_s\sqrt{\pi/G\rho_0}$, indicates the turning scale of the density fluctuation evolution.

On large scales where pressure term can be negligible (equivalently, enough larger than the Jeans length) we can rewrite eq. (2.37) as

$$\ddot{\delta} + \frac{2\dot{a}}{a} \dot{\delta} - 4\pi G\rho_0 \delta = 0. \quad (2.38)$$

Since this equation does not contain any wavenumber, eq. (2.38) holds both in real and in Fourier spaces and the density fluctuations evolve independent of k . Equation (2.38) can

be solved analytically and the solutions are known as the growing and decaying modes as

$$D_+ \propto H \int \frac{da}{a^3 H^3} \quad : \text{growing mode} \quad (2.39)$$

$$D_- \propto H \quad : \text{decaying mode.} \quad (2.40)$$

and D_+ has the exact integral expression as

$$D_+ = \frac{5}{2} a \Omega_m \int_0^1 (\Omega_m/x + \Omega_\Lambda x^2 + \Omega_K)^{-3/2} dx \quad (2.41)$$

where the normalization is set by $\lim_{a \rightarrow 0} D_+ = a$. Note that a convenient calculation formula is also known as follows:

$$D_+ \sim \frac{5}{2} a \Omega_m \left[\Omega_m^{4/7} - \Omega_\Lambda + \left(1 + \frac{\Omega_m}{2} \right) \left(1 + \frac{\Omega_\Lambda}{70} \right) \right]^{-1}. \quad (2.42)$$

Next I consider evolution of the velocity field. Taking the rotation of eq. (2.32), we get

$$\left(\frac{\partial}{\partial t} + H \right) \nabla \times \mathbf{u} = 0. \quad (2.43)$$

This equation means that the rotation of velocity field decays as a^{-1} . Thus with proper velocity potential Ψ , the velocity field can be expressed as

$$\mathbf{u} = -\frac{\nabla \Psi}{aH}. \quad (2.44)$$

Combining eq. (2.33) and divergence of eq. (2.44), second derivative of velocity potential becomes

$$\nabla^2 \Psi = a^2 H \dot{\delta} = a^2 H^2 f \delta \quad (2.45)$$

$$f = \frac{d \ln D}{d \ln a} = \frac{\dot{D}}{HD}, \quad D = \frac{D_+(t)}{D_+(t_0)} \quad (2.46)$$

where f is the linear growth rate that relates the density fluctuations with the velocity field and D the linear growth factor. Thus the linear density field at z is written with D as

$$\delta(k, z) = \frac{D(z)}{D(z=0)} \delta(k, z=0). \quad (2.47)$$

The value of linear growth rate f can be evaluated by derivative of D , for Λ CDM universe it is

$$f = -1 - \frac{\Omega_m}{2} + \Omega_\Lambda + \left[\int_0^1 \frac{dx}{(\Omega_m/x + \Omega_\Lambda x^2 + 1 - \Omega_K)^{3/2}} \right]^{-1} \quad (2.48)$$

or employing approximate formula:

$$f \sim \Omega_m^{4/7} + \frac{\Omega_\Lambda}{70} \left(1 + \frac{\Omega_m}{2} \right). \quad (2.49)$$

For the case of Einstein-de Sitter universe $f = 1$ without any time dependence.

By comparing eqs. (2.35) and (2.45), velocity and gravitational potentials are related as

$$\Psi = \frac{H^2 f}{4\pi G \bar{\rho}} \Phi. \quad (2.50)$$

thus through easy calculation we can derive following expressions:

$$\tilde{\Psi}(\mathbf{k}, t) = -\frac{a^2 H^2 f}{k^2} \tilde{\delta}(\mathbf{k}, t) \quad (2.51)$$

$$\Psi(\mathbf{x}, t) = -\frac{a^2 H^2 f}{4\pi} \int d^3 x' \frac{\delta(\mathbf{x}', t)}{|\mathbf{x} - \mathbf{x}'|} \quad (2.52)$$

and

$$\tilde{\mathbf{u}}(\mathbf{k}, t) = aHf \frac{i\mathbf{k}}{k^2} \tilde{\delta}(\mathbf{k}, t) \quad (2.53)$$

$$\mathbf{u}(\mathbf{x}, t) = -\frac{aHf}{4\pi} \int d^3 x' \frac{\mathbf{x} - \mathbf{x}'}{|\mathbf{x} - \mathbf{x}'|^3} \delta(\mathbf{x}', t). \quad (2.54)$$

2.3 LSS statistics

It is hard to predict density contrast at an arbitrary position $\delta(\mathbf{x})$ since the fluctuation is stochastic quantity. However the correlation of the fluctuations at two points separated a given distance, named as two point correlation function, or its Fourier partner, the power spectrum are available to discuss the amplitude fluctuation growth. Note that, although these are mathematically equivalent statistics, both are used complementary because each of these has its merits and demerits, e.g., difficulty of including survey geometry effects and calculation time in measuring these statistics.

2.3.1 Correlation function and power spectrum

Two point correlation function

Two point correlation function is more intuitive quantity than the power spectrum, which gives how correlation is strong or weak compared to the average. It is defined as the ensemble average of product of fluctuations at two points separated a given distance:

$$\xi(r) = \langle \delta(\mathbf{x}_1) \delta(\mathbf{x}_2) \rangle, \quad (2.55)$$

where $r = |\mathbf{x}_1 - \mathbf{x}_2|$. In terms of number density of observed galaxies, n , and its average, \bar{n} , the correlation function is also expressed as

$$\langle n(\mathbf{x}_1) n(\mathbf{x}_2) \rangle = \bar{n}^2 [1 + \xi(r)] \quad (2.56)$$

If any point has no correlation with all the other points, by definition, correlation function becomes $\xi(r) = 0$. Due to gravitational instability, the correlation function has positive values at small r , and integration of eq. (2.55) over r with fixed \mathbf{x}_1 becomes

$$\int_0^\infty dr r^2 \xi(r) = 0, \quad (2.57)$$

since $\langle \delta(\mathbf{x}) \rangle = 0$. From (2.57), there exists r_s that $\xi(r_s) = 0$ and this value is called as correlation length.

Power spectrum

The squared value of the Fourier transform of the density fluctuation $\tilde{\delta}_{\mathbf{k}}$ is called as the power spectrum:

$$P(\mathbf{k}) = \langle |\tilde{\delta}_{\mathbf{k}}|^2 \rangle \quad (2.58)$$

and known as a readily handling statistic, since $\tilde{\delta}_{\mathbf{k}}$ grows k -independently. Here, let me lead relation of the power spectrum with the correlation function. If considering the ensemble average of the product of different wavevector density fluctuations:

$$\begin{aligned} \langle \tilde{\delta}_{\mathbf{k}} \tilde{\delta}_{\mathbf{k}'} \rangle &= \frac{1}{(2\pi)^6} \int d^3x_1 d^3x_2 \xi(|\mathbf{x}_1 - \mathbf{x}_2|) e^{-i\mathbf{k} \cdot \mathbf{x}_1 - i\mathbf{k}' \cdot \mathbf{x}_2} \\ &= \frac{1}{(2\pi)^6} \int d^3x_1 d^3x \xi(|\mathbf{x}|) e^{-i(\mathbf{k} + \mathbf{k}') \cdot \mathbf{x}_1 + i\mathbf{k}' \cdot \mathbf{x}} \\ &= \frac{1}{(2\pi)^3} \int d^3x \xi(|\mathbf{x}|) e^{-i\mathbf{k}' \cdot \mathbf{x}} \delta^{(3)}(\mathbf{k} + \mathbf{k}') \end{aligned} \quad (2.59)$$

by using replacement of $\mathbf{x} = \mathbf{x}_1 - \mathbf{x}_2$. Integrating both sides over \mathbf{k}' , since density fluctuation is real valued function $\tilde{\delta}_{-\mathbf{k}} = \tilde{\delta}_{\mathbf{k}}^*$ holds then l.h.s becomes $P(\mathbf{k})$. We get following equation

$$P(\mathbf{k}) = \frac{1}{(2\pi)^3} \int d^3x \xi(|\mathbf{x}|) e^{-i\mathbf{k} \cdot \mathbf{x}}. \quad (2.60)$$

This is known as Wiener-Khinchin's relation.

2.3.2 Evolution of the power spectrum

It is important to understand the initial power spectrum properly because both of the amplitude and shape of the power spectrum at present strongly reflect those of the initial power spectrum.

Using eq. (2.47), the linear power spectrum can be written as

$$P_{\text{lin}}(k, z) = \frac{D^2(z)}{D^2(z_{\text{init}})} P_{\text{init}}(k) \quad (2.61)$$

where $P_{\text{init}}(k)$ is the power spectrum at an appropriate high redshift z_{init} when the density fluctuation is enough small. Theoretically $P_{\text{init}}(k)$ is derived by solving some simultaneous evolution equations of the density fluctuation including physical processes of gravity interaction, pressure and dissipation. The solution for these equations is called the transfer function and needs to be found numerically. Fortunately there is a publicly available code for this calculation ‘‘Code for Anisotropies in the Microwave Background’’ (CAMB, [48]), and we uses this code to calculate P_{init} .

There still exists a freedom of the amplitude of the power spectrum and it is to be observationally determined. Here the mass fluctuation can related to the power spectrum

as follows: Concerning a point and the sphere region of a radius R around it, the mass fluctuation becomes

$$\frac{\delta M}{\bar{M}} = \frac{3}{4\pi R^3} \int_{|\mathbf{x}| < R} d^3x \delta(\mathbf{x}) = \int d^3x \delta(\mathbf{x}) W(\mathbf{x}) \quad (2.62)$$

where $\bar{M} = 4\pi R^3 \rho_0 / 3$ and $W(\mathbf{x})$ is the top hat window function:

$$W(\mathbf{x}) = \frac{3}{4\pi R^3} \Theta(R - |\mathbf{x}|) \quad (2.63)$$

$$\Theta(x) = \begin{cases} 1 & (x \geq 0) \\ 0 & (x < 0) \end{cases} . \quad (2.64)$$

Then, its dispersion σ_R^2 is

$$\begin{aligned} \sigma_R^2 &= \left\langle \left(\frac{\delta M}{\bar{M}} \right)^2 \right\rangle \\ &= \int d^3x_1 d^3x_2 \langle \delta(\mathbf{x}_1) \delta(\mathbf{x}_2) \rangle W(\mathbf{x}_1) W(\mathbf{x}_2) \\ &= \int d^3k P(\mathbf{k}) |\widetilde{W}_{\mathbf{k}}|^2 \end{aligned} \quad (2.65)$$

where $\widetilde{W}_{\mathbf{k}}$ is the Fourier transform of the window function, here I use following relation from eq. (2.59)

$$\langle \widetilde{\delta}_{\mathbf{k}} \widetilde{\delta}_{\mathbf{k}'} \rangle = (2\pi)^3 \delta^{(3)}(\mathbf{k} + \mathbf{k}') P(\mathbf{k}') . \quad (2.66)$$

Assuming the isotropic universe, eq. (2.65) can be further reformed as

$$\sigma_R^2 = \int \frac{k^2 dk}{2\pi^2} P(k) |\widetilde{W}_{kR}|^2 \quad (2.67)$$

where

$$\widetilde{W}_{kR} = \frac{3}{(kR)^3} [\sin(kR) - kR \cos(kR)] . \quad (2.68)$$

Fig. 2.1 shows the behavior of this function, which filters out the power spectrum at $k > R^{-1}$. Thus σ_R^2 is a quantity that reflects the longer than the scale R . It is often used the value on $8 h^{-1} \text{Mpc}$ at $z=0$, σ_8 , as a normalization of the power spectrum. Since there is no theory that predicts σ_8 value, this is determined observationally.

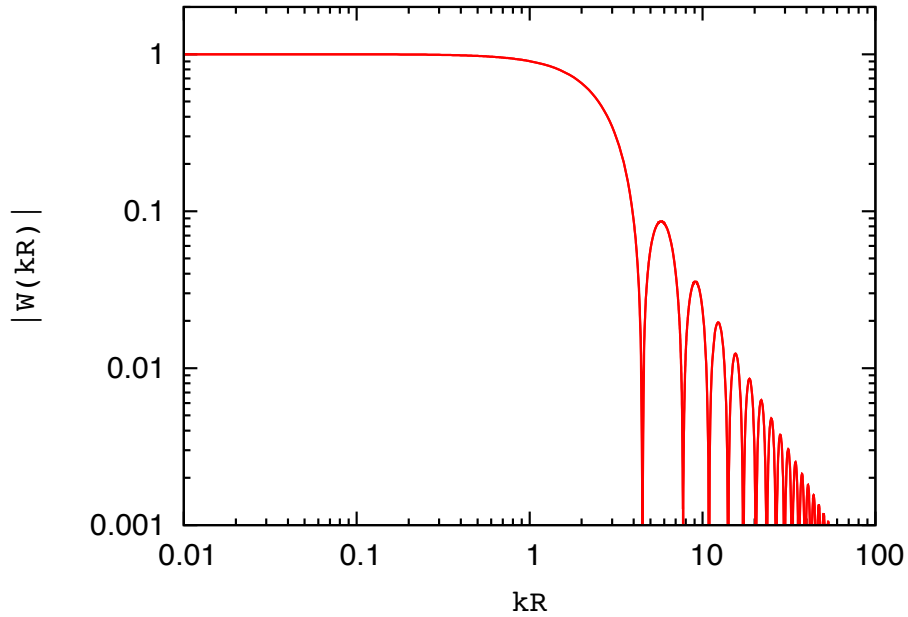


Fig. 2.1. The window function eq. (2.68). One can easily see that this function drops down abruptly where $k > 1/R$ and this filters out the power spectrum signals on small scales.

2.4 2D power spectrum in redshift space

As I mentioned in section 1.2 because of peculiar velocities of galaxies, their distribution distorts along line-of-sight direction. In this section, I explain the power spectrum in redshift space.

2.4.1 Linear formula of RSD

On large scales of linear region, the positions of haloes (or matter) are shifted along the line-of-sight coordinate as

$$\mathbf{s} = \mathbf{x} + \frac{v_z}{aH} \hat{z} \quad (2.69)$$

under the plane-parallel approximation, where \mathbf{s} is the redshift-space coordinate, \mathbf{x} the real-space counterpart, $v_z = au_z$ peculiar velocity of halo (matter) whereas \hat{z} denotes the unit vector along the line of sight. The total number of galaxy number conserves:

$$\int d^3s n_s = \int d^3x n_r \quad (2.70)$$

where n_s and n_r shows the number density of galaxies in redshift space and in real space, respectively. Since the averages of these densities are the same, their fluctuations are

related as

$$d^3s (1 + \delta^s) = d^3x (1 + \delta) \quad (2.71)$$

where δ^s is the density fluctuation in redshift space. Thus we can write this equation as

$$\delta^s(\mathbf{s}) = \left| \frac{\partial \mathbf{s}}{\partial \mathbf{r}} \right|^{-1} \{1 + \delta\} - 1 \quad (2.72)$$

where $|\partial \mathbf{s} / \partial \mathbf{r}|$ is the Jacobian. In linear theory, the higher order term of l.h.s. is negligible and can be replaced with $\delta^s(\mathbf{x})$. Taking the Fourier transform on this equation, we get

$$\tilde{\delta}_{\mathbf{k}}^s = \tilde{\delta}_{\mathbf{k}} - \frac{ik_z}{aH} \tilde{v}_z \quad (2.73)$$

and by using eq. (2.53) we get the Kaiser formula:

$$P^s(k, \mu) = (1 + \beta \mu^2)^2 P_{\text{lin}}(k) \quad (2.74)$$

where l.h.s. is the 2D power spectrum in redshift space, β RSD parameter defined as $\beta = f/b$, $\mu = k_z/|\mathbf{k}|$ the direction cosine between the wavevector and line-of-sight, and $P_{\text{lin}}(k)$ the linear power spectrum. Hereafter I abbreviate superscript letter “s” on the 2D power spectrum $P(k, \mu)$.

2.4.2 Non-linear RSD model

By using the fact that the Jacobian is written as $1 + \nabla_z v_z / (aH)$. The Fourier transform of eq. (2.72) gives

$$\delta^s(\mathbf{k}) = \int d^3\mathbf{r} \left\{ \delta(\mathbf{r}) - \frac{\nabla_z v_z(\mathbf{r})}{aH(z)} \right\} e^{i(k\mu v_z/H + \mathbf{k} \cdot \mathbf{r})}. \quad (2.75)$$

Then the exact expression of the Fourier transform is given by squaring eq. (2.75) as:

$$P^s(\mathbf{k}) = \int d^3\mathbf{x} e^{i\mathbf{k} \cdot \mathbf{x}} \langle e^{-ik\mu f \Delta u_z} \times \{ \delta(\mathbf{r}) + f \nabla_z u_z(\mathbf{r}) \} \{ \delta(\mathbf{r}') + f \nabla_z u_z(\mathbf{r}') \} \rangle \quad (2.76)$$

[35], where $\mathbf{x} = \mathbf{r} - \mathbf{r}'$, $u_z(\mathbf{r}) = -v_z(\mathbf{r})/(aHf)$ and $\Delta u_z = u_z(\mathbf{r}) - u_z(\mathbf{r}')$.

Proper account of the non-linear effect has been discussed with employing perturbative treatment of the evolutions of the density and velocity fields (see, [35, 49]), and a non-linear model of Kaiser effect was proposed as

$$P(k, \mu) = P_{\delta\delta}(k) + 2f\mu^2 P_{\delta\theta}(k) + f^2\mu^4 P_{\theta\theta} \quad : \text{non-linear} \quad (2.77)$$

where $P_{\delta\delta}$, $P_{\delta\theta}$ and $P_{\theta\theta}$ are the non-linear auto power spectra of density and velocity divergence, $\theta = \nabla \cdot \mathbf{u}$, and the non-linear cross power spectrum of density-velocity divergence, respectively. Furthermore [37] derives the higher order correction terms and suggested an improved prescription for the 2D power spectrum as

$$P(k, \mu) = D_{\text{FoG}}(k\mu f \sigma_v) \times [P_{\delta\delta}(k) + 2f\mu^2 P_{\delta\theta}(k) + f^2\mu^4 P_{\theta\theta}(k) + A(k, \mu; f) + B(k, \mu; f)] \quad (2.78)$$

with

$$D_{\text{FoG}}(x) = \begin{cases} \exp(-x^2) & : \text{Eulerian} \\ 1/(1+x^2/2)^2 & : \text{Lorentzian} \end{cases}, \quad (2.79)$$

$$A(k, \mu; f) = (k\mu f) \int \frac{d^3\mathbf{p}}{(2\pi)^3} \frac{p_z}{p^2} \{B_\sigma(\mathbf{p}, \mathbf{k} - \mathbf{p}, -\mathbf{k}) - B_\sigma(\mathbf{p}, \mathbf{k}, -\mathbf{k} - \mathbf{p})\}, \quad (2.80)$$

$$B(k, \mu; f) = (k\mu f)^2 \int \frac{d^3\mathbf{p}}{(2\pi)^3} F(\mathbf{p})F(\mathbf{k} - \mathbf{p}) \quad (2.81)$$

where B_σ is the cross bispectrum defined as

$$\begin{aligned} & \left\langle \theta(\mathbf{k}_1) \left\{ \delta(\mathbf{k}_2) + f \frac{k_{2z}^2}{k_2^2} \theta(\mathbf{k}_2) \right\} \left\{ \delta(\mathbf{k}_3) + f \frac{k_{3z}^2}{k_3^2} \theta(\mathbf{k}_3) \right\} \right\rangle \\ & = (2\pi)^3 \delta_D(\mathbf{k}_1 + \mathbf{k}_2 + \mathbf{k}_3) B_\sigma(\mathbf{k}_1, \mathbf{k}_2, \mathbf{k}_3), \end{aligned} \quad (2.82)$$

the Kernel $F(\mathbf{p})$ as

$$F(\mathbf{p}) = \frac{p_z}{p^2} \left\{ P_{\delta\theta}(p) + f \frac{p_z^2}{p^2} P_{\theta\theta}(p) \right\} \quad (2.83)$$

and σ_v in the damping function is the 1D velocity dispersion and to be determined by fitting the model to the N-body simulations. We call this model eq.(2.78) as ‘‘the TNS model’’.

2.5 Galaxy/halo bias

2.5.1 Galaxy bias problem

It is widely known that the fluctuation of number density of observed galaxies does not trace that of background matter distribution, although some relations would be expected between them. Therefore the power spectrum for observed galaxies cannot be modeled by or compared with the matter power spectrum straightforwardly and this is known as galaxy bias problem. Historically, the exist of bias was discovered by [50] through the work of N-body simulation. They found the slope of the matter correlation function measured from simulation are not consistent with that of observed galaxies. Note that their simulation was performed in the Einstein-de Sitter universe with $\Omega_m = 1$. Although a low- Ω universe simulation eases this mismatch more or less, proper treatment of the bias is still needed as the correlation function (or the power spectrum) to be an amplified version of that for matter. [51] suggested the high-peak model that bright galaxies exist at the high peaks in the initial density field and modeled the linear bias as

$$\delta_{\text{gal}} = b\delta_m, \quad (2.84)$$

and this can describe observed data well on large scales. In the most simple case one assumes b as a constant, but in general, the bias is the function of the wavenumber as $b = b(k)$.

2.5.2 RSD formulae for halo power spectrum

Combining the galaxy bias, the Kaiser formula eq. (2.74) for the galaxy power spectrum becomes

$$P_{\text{gal}}(k, \mu) = b^2(1 + \beta\mu^2)^2 P_{\text{lin}}(k). \quad (2.85)$$

From redshift survey data, we can measure two independent parameters of $b\sigma_8$ from the amplitude of the galaxy power spectrum and RSD parameter $\beta = f/b$ from anisotropy of it. Though the galaxy bias would have the scale-dependence, by multiplying these parameters we can cancel the systematic arising from the uncertainty of the galaxy bias. Therefore the linear growth parameter $f\sigma_8$ becomes an observable only from galaxy surveys (see Fig. 2.2).

[38] extended the TNS model for the halo power spectrum with the assumption of linear bias and suggested

$$P_{\text{halo}}^s(k, \mu) = D_{\text{FoG}}(k\mu f \sigma_v) \times b^2 [P_{\delta\delta}(k) + 2\beta\mu^2 P_{\delta\theta}(k) + \beta^2\mu^4 P_{\theta\theta}(k) + bA(k, \mu; \beta) + b^2B(k, \mu; \beta)]. \quad (2.86)$$

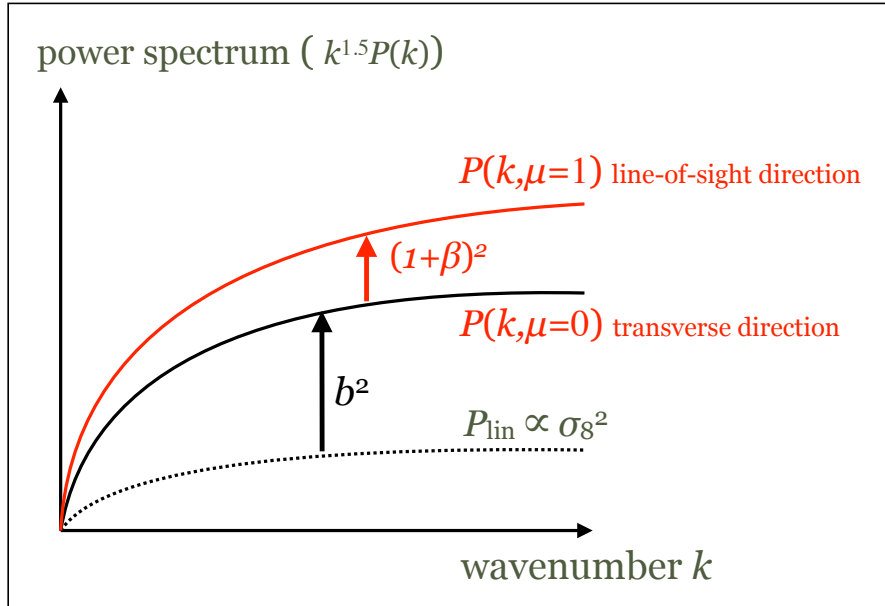


Fig. 2.2. Laugh illustration of the relation between 2D halo power spectrum and the matter power spectrum in the real space for the linear Kaiser RSD view. The halo power spectrum in transverse direction (black solid line) (equivalently, the real space halo power spectrum) is the enhanced version of the matter one (black dotted line) by b^2 , and the line-of-sight direction halo power spectrum can be related with the transverse direction one by RSD parameter β .

Chapter 3

N-body simulation, mock catalog generation and power spectrum measurements

In this chapter I will describe the details of cosmological N-body simulation that we carried out, and of the power spectrum measurements for matter and haloes. We are mainly interested in RSD analysis for haloes though, we also analysed the matter power spectrum because there is no halo bias and it may help us to better understand where the systematic errors come from in RSD measurements. In addition to this, the subhalo power spectrum was examined to check if our halo identify algorithm used in this study is plausible or not.

3.1 N-body simulation with Gadget2

For our N-body simulation, I used the public code for cosmological simulation `GADGET2` [52, 53]. In our paper [54], I employed $N_p = 1024^3$ DM particles in a cubic box of $700 h^{-1} \text{Mpc}$ on a side with periodic boundary conditions. This gives the mass resolution (namely, the mass of one DM particle) of $2.4 \times 10^{10} h^{-1} M_\odot$. `GADGET2` parameters regarding force and time integration accuracy are as follows: `PMGRID=20483`, `MaxSizeTimestep=0.03`, `MaxRMSDisplacementFac=0.25` and `ErrTolForceAcc=0.001`. The gravitational softening length is set to be 4 per cent of the mean inter-particle distance. Note that compared with the halo power spectrum from higher-mass resolution simulation (i.e., $N_p = 1280^3$ and 1535^3), our resolution choice is sufficient to resolve haloes we identified, in which we assume galaxies exist (please see, Fig. 3.1 in subsection 3.3.1). In addition, `Gadget2` parameters are also confirmed to be sufficient for generating halo catalog by comparing the power spectrum with those from higher-accuracy setting simulations.

We prepared the initial linear power spectrum at redshift $z_{\text{init}} = 49$ by using code `CAMB` which is based on Boltzmann solver code and computes matter transfer function. Then initial conditions of our simulations were generated using parallel `2LPT` code which uses the second order Lagrangian perturbation theory [55, 56]. We ran a total of 40 realisations with different random seeds to reduce statistical errors on the power spectrum and investigate the systematic errors on the $f\sigma_8$ measurements precisely. The snapshots are dumped at three redshifts $z = 2, 1.35$ and 0.5 for each realisation.

Table. 3.1. Summary of the halo catalogues. The minimum mass M_{\min} and the mean halo mass $\overline{M}_{\text{halo}}$ are shown in units of $h^{-1}M_{\odot}$, and the halo number density n_{halo} is shown in $h^3\text{Mpc}^{-3}$. The halo bias shows the value of $b_0\sigma_8/\sigma_{8,\text{input}}$, where b_0 and σ_8 are the best-fitting parameters by fitting with the TNS+Q-model bias.)

$z=2$				$z=1.35$			$z=0.5$		
M_{\min}	$\overline{M}_{\text{halo}}$	n_{halo}	bias	$\overline{M}_{\text{halo}}$	n_{halo}	bias	$\overline{M}_{\text{halo}}$	n_{halo}	bias
5.0×10^{11}	1.51×10^{12}	4.52×10^{-3}	2.3	1.92×10^{12}	6.15×10^{-3}	1.7	2.83×10^{12}	7.43×10^{-3}	1.1
1.0×10^{12}	2.65×10^{12}	1.91×10^{-3}	2.6	3.32×10^{12}	2.96×10^{-3}	1.9	4.90×10^{12}	3.77×10^{-3}	1.2
2.0×10^{12}	4.61×10^{12}	7.52×10^{-4}	3.1	5.71×10^{12}	1.28×10^{-3}	2.2	8.36×10^{12}	1.90×10^{-3}	1.4
5.0×10^{12}	9.80×10^{12}	1.80×10^{-4}	3.9	1.19×10^{13}	3.90×10^{-4}	2.7	1.70×10^{13}	7.22×10^{-4}	1.7
1.0×10^{13}	1.74×10^{13}	5.14×10^{-5}	4.7	2.08×10^{13}	1.42×10^{-4}	3.3	2.90×10^{13}	3.30×10^{-4}	1.9
2.0×10^{13}	3.13×10^{13}	1.16×10^{-5}	6.1	3.66×10^{13}	4.43×10^{-5}	4.0	4.96×10^{13}	1.40×10^{-4}	2.3

3.2 Halo identification

Halo identification is performed by Friends-of-Friends (FoF) algorithm incorporated in `Gadget2`. This algorithm assumes that DM particles separated by less than linking length parameter b_F with respect to mean inter particle separation are hosted in the same halo. We set this parameter to $b_F = 0.2$, which is the often used value in N-body simulation studies, and the hosts contain at least 20 linked particles were identified as haloes. By varying the minimum mass threshold of for haloes in the range of $5.0 \times 10^{11} - 2.0 \times 10^{13} h^{-1}M_{\odot}$, we made six different halo mass catalogues at each redshift. Detailed properties of our halo catalogues including mean halo masses, $\overline{M}_{\text{halo}}$, and halo number densities, n_{halo} , are shown in Table 3.1.

Note that the FoF algorithm can catch unbound DM particles with large velocity by chance, we found subhaloes from identified haloes by using subhalo finder `subfind` [57, 58], which calculates gravitational potential of the particles in a halo and regroups particles when they are gravitationally bound to each other as subhaloes.. Here we treat a group consisting more than 10 particle as subhalo, and we call the most massive subhalo in each halo as *central*. Although the measured power spectra for central subhaloes are differ from the halo power spectra by a few per cent level, they gives consistent $f\sigma_8$ estimates with FoF haloes within 1 per cent level. Thus we conclude that the FoF algorithm as a halo identifier is reliable for our purpose.

3.3 Power spectrum measurement

3.3.1 2D power spectrum

Here I explain how to measure the 2D power spectra, $P_{\text{sim}}(k, \mu)$. To measure the power spectrum for the simulated matter distribution and for halo catalogues in redshift space, I used the standard method based on the Fourier transform as follows. Firstly, the positions of DM particles or haloes are shifted along the line-of-sight coordinate as $\mathbf{s} = \mathbf{x} + v_z/(aH)\hat{z}$ under the plane-parallel approximation, where \mathbf{s} is the redshift-space coordinates, \mathbf{x} the real-space counterpart, and \hat{z} the unit vector along the line-of-sight. (Of course, when we measure the real-space spectrum, we use only \mathbf{x} and $P_{\text{sim}}(k, \mu)$ becomes the 1D isotropic

power spectrum $P_{\text{sim}}(k)$.) Secondly, the shifted positions of matter (or haloes) are assigned onto regular 1280^3 grids through the clouds-in-cells (CIC) interpolation scheme. Then, I calculated the fluctuations of number density $\delta(\mathbf{s})$ on each grid and performed discrete Fourier transform on them with deconvolution of the smoothing kernel of CIC [59, 60, 61]. For the density fluctuation in Fourier space, the power spectrum for a given realisation can be estimated as

$$\hat{P}(k, \mu) = \frac{1}{N_{\text{mode}}} \sum_{\mathbf{k}} |\delta_{\mathbf{k}}|^2 - P_{\text{shot}} \quad (3.1)$$

where the summation is taken over N_{mode} Fourier modes in a (k, μ) bin. Here we choose the size of bin as $\Delta k = 0.01 h\text{Mpc}^{-1}$ for the wavenumber and $\Delta\mu = 0.1$ for the direction cosine. In the above equation, P_{shot} denotes the shot noise term, which arises from the self-correlation of the individual haloes, and its expected value is the inverse of the halo number density, n_{halo}^{-1} . Note that the matter power spectrum estimation, we do not subtract the shot noise. Strictly speaking, this binned power spectrum can deviate from the true ensemble average due to the wavenumber discreteness and to the finiteness of the simulation volume. To overcome these difficulties, finally, we averaged the 40 independent power spectra as $P_{\text{ave40}}(k, \mu) = \langle \hat{P}(k, \mu) \rangle$ for matter and haloes, where the bracket $\langle \dots \rangle$ stands for the ensemble average ^{*1}.

In Fig. 3.1, I show the measured 2D halo power spectra $\hat{P}(k, \mu)$ at $z = 1.35$ for haloes with the mass threshold of $M_{\text{min}} = 5.0 \times 10^{11} h^{-1} M_{\odot}$. The plot shows the power spectra at three direction cosine values $\mu = 0.05, 0.55$ and 0.95 from bottom to top, respectively, from different mass resolution simulations (i.e., $N_p = 1024^3, 1280^3$ and 1536^3 , see labels). We confirm that our mass resolution employing 1024^3 particles is efficient to generate halo catalogues with $M_{\text{min}} \gtrsim 5.0 \times 10^{11} h^{-1} M_{\odot}$.

^{*1} The measured power spectra, both real-space $P^{\text{real}}(k)$ and redshift-space 2D $P(k, \mu)$, are publicly released in <http://www.kusastro.kyoto-u.ac.jp/~ishikawa/catalogues/>

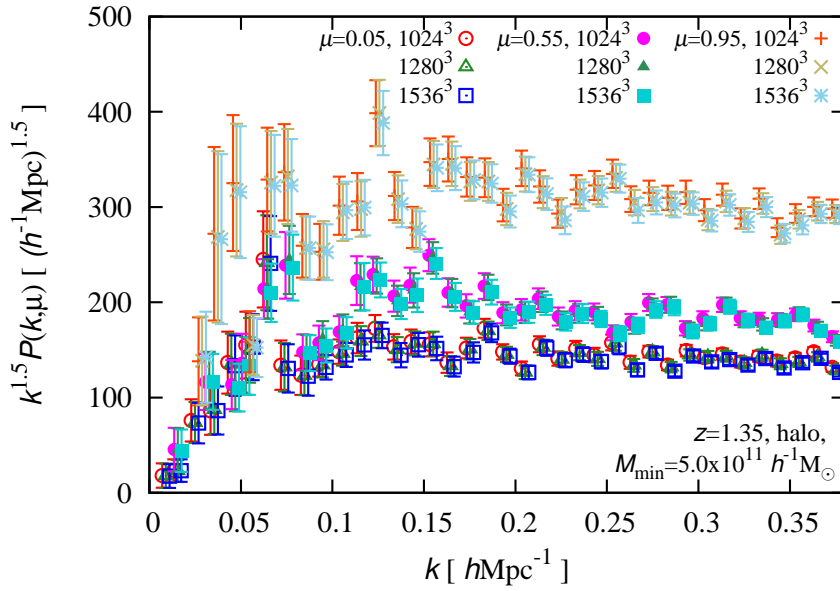


Fig. 3.1. The measured 2D power spectra in redshift space for halo catalogues of $M_{\min} = 5.0 \times 10^{11} h^{-1} M_{\odot}$ at $z = 1.35$. Open, filled and plus (cross, star) symbols show the power spectra at $\mu = 0.05, 0.55$ and 0.95 , respectively. For the same μ value, three types of points show the power spectra for different mass resolution simulations with $N_p = 1024^3, 1280^3$ and 1536^3 from left to right, respectively. Error bars show FKP error estimated as $(\hat{P} + P_{\text{shot}})/\sqrt{N_{\text{mode}}}$ [62]. All the data points are on the same k grids but they are slightly shifted horizontally around the true k values for clarity.

Chapter 4

Analysis and Results

4.1 Parameter estimation analysis

In this section I explain how do we measure linear growth parameter, $f\sigma_8$, from the 2D power spectrum in redshift space. We used four theoretical models for the halo 2D power spectrum in the study: combinations of two types of analytical models for the 2D power spectrum with two parametrizations of the halo bias. To estimate the best-fitting model parameters and statistical errors on them, we employed the Markov-chain-Monte-Carlo (MCMC) method.

4.1.1 Fitting model and model parameters

In the linear theory, the 2D halo power spectrum in redshift space is modeled as

$$P(k, \mu) = b^2(1 + \beta\mu^2)^2 P_{\text{lin}}(k) \quad (4.1)$$

[11]. To incorporate the FoG effect arising from halo velocity dispersion, we multiplied the Lorentzian-type damping function to eq. (4.1):

$$P(k, \mu) = D_{\text{FoG}}(k\mu f\sigma_v) \times b^2(1 + \beta\mu^2)^2 P_{\text{lin}}(k) \quad (4.2)$$

where $D_{\text{FoG}}(x) = 1/(1 + x^2/2)^2$ [31]. Eq. (4.2) is called as “the Kaiser model” hereafter. We also tested “the TNS model” derived by [37, 38]:

$$P(k, \mu) = D_{\text{FoG}}(k\mu f\sigma_v) \times b^2 \left[P_{\delta\delta}(k) + 2\beta\mu^2 P_{\delta\theta}(k) + \beta^2\mu^4 P_{\theta\theta}(k) + bC_A(k, \mu; \beta) + b^2 C_B(k, \mu; \beta) \right] \quad (4.3)$$

(See also sections 2.4 and 2.5).

For the halo bias, we assumed a linear bias $b = \delta_{\text{halo}}/\delta_{\text{m}}$, and tested two bias models: a constant bias and a empirical “Q-model bias” to allow scale-dependence [17, 38] which are expressed as

$$b(k) = \begin{cases} b_0 & : \text{constant bias} \\ b_0 \sqrt{\frac{1 + Qk^2}{1 + Ak}} & : \text{Q-model bias,} \end{cases} \quad (4.4)$$

where b_0 , Q and A are fitting parameters.

To summarize, we tested the following four theoretical models for the 2D halo power spectrum in redshift space: “Kaiser+constant bias”, “Kaiser+Q-model bias”, “TNS+constant bias” and “TNS+Q-model bias” in this study. Note that since the TNS model was originally developed for the non-linear matter power spectrum and expanded to the halo power spectrum, eq. (4.3) is only valid for the *constant* halo bias (see [38]). Therefore there is an inconsistency in incorporating the Q-bias model bias with the TNS model, nevertheless this is probably the best approach available for the moment. Assuming that one cannot measure the amplitude of the matter power spectrum from any galaxy surveys, we treated σ_8 as a free parameter in fitting analysis. Eventually, all the four models include four parameters, f, b_0, σ_v and σ_8 , and extra two bias parameters, Q and A for the models embedded with the scale-dependent Q-model bias.

Before analysis we prepare templates for the power spectrum of eqs. (4.1) and (4.3) at each of the three redshifts with a fiducial (simulation input) cosmological parameters. In particular, the three non-linear power spectra, $P_{\delta\delta}$, $P_{\delta\theta}$ and $P_{\theta\theta}$, are calculated by using the closure approximation up to the second-order Born approximation, and the correction terms, C_A and C_B , are evaluated by the one-loop standard perturbation theory [63, 64, 37]. Note that σ_8 , which is not explicit parameter in eqs. (4.1) and (4.3), is dealt with by re-scaling the template spectra as follows. We replace the density and velocity spectra as $P_{ab} \rightarrow P_{ab} \times (\sigma_8(z)/\sigma_{8,\text{input}}(z))^2$ and the correction terms as C_A (or C_B) $\rightarrow C_A$ (or C_B) $\times (\sigma_8(z)/\sigma_{8,\text{input}}(z))^4$, where $\sigma_{8,\text{input}}(z) = D(z)\sigma_{8,\text{fid}}$ and $\sigma_{8,\text{fid}} = 0.81$. These replacements are valid at the leading order, and we expect that the error induced by this approximated treatment would be small. This procedure significantly saves computing time to calculate the spectra for a suggested σ_8 value in MCMC chains compared to recalculate power spectrum templates each by each.

4.1.2 MCMC technique

MCMC is one of the most popular methods based on maximum likelihood estimation to find the distributions of the model parameters, namely best-fitting values and allowed regions of them. An MCMC chain, which the method generates, contains a sequence of parameter sets as samples, therefore the chain itself represents the distributions of parameters. The following shows how to generate the MCMC chain:

1. Set a start parameter set θ_0 (arbitrary).

and iterate 2–4 for each t

2. Generate a candidate parameter set $\tilde{\theta}_{t+1}$ for the next sample by pickup a point in some neighbor region of θ_t
3. Calculate χ^2 values for the sets θ_t and $\tilde{\theta}_{t+1}$.
4. Decide whether or not to accept a candidate with the likelihood ratio defined as $\alpha = \mathcal{P}(\tilde{\theta}_{t+1})/\mathcal{P}(\theta_t)$ where $\mathcal{P}(\theta_t) \propto \mathcal{L}(\theta_t) = \exp[-\chi^2(\theta_t)/2]$.
 - (a) When $\alpha \geq 1$, (equivalently, $\tilde{\theta}_{t+1}$ is more likely than θ_t) then accept the candidate automatically and set $\theta_{t+1} = \tilde{\theta}_{t+1}$.
 - (b) Otherwise, accept the candidate with probability α and set $\theta_{t+1} = \tilde{\theta}_{t+1}$; if the candidate is rejected, keep $\theta_{t+1} = \theta_t$ instead.

After enough steps, the chain should be expected to converge to the desired parameter distribution. I employed a Gelman-Rubin diagnostic test [65] to check the chain convergence.

The Gelman-Rubin statistic is defined with using subchain statistics as

$$\hat{R} = \left(\frac{k-1}{k} W + B \right) / W \quad (4.5)$$

$$W = \frac{1}{n} \sum_{i=1}^n s_i^2, \quad B = \frac{1}{n-1} \sum_{i=1}^n (\mu_i - \bar{\mu})^2 \quad (4.6)$$

where k is the subchain length, n the number of subchains, μ_i and s_i^2 are the average and unbiased variance of i -th subchain and $\bar{\mu} = \langle \mu_i \rangle$. (In original paper they suggest using the square root of eq. (4.5), $\sqrt{\hat{R}}$, is as an estimator.) When the MCMC chain is enough long, the averages of subchains μ_i are expected to approach $\bar{\mu}$, therefore the convergence of the chain can be evaluated by \hat{R} value. In our analysis, we choose $n = 5$ and MCMC chains were generated enough long to pass Gelman-Rubin test with condition $\hat{R} < 1.05$ for all the model parameters.

4.1.3 Wilson-Hilferty approximation

In our analysis, we tried to fit the shape of the 2D power spectrum, $P_{\text{sim}}(k, \mu)$ directly, in contrast to the analyses using the ratio of the multipole moments [66, 29]. In such a case, one faces difficulties arising from that there is only a small numbers of Fourier modes in a (k, μ) bin. The likelihood can be written as $L \propto \exp(-\chi^2/2)$, with the assumption that a measured power spectrum $P(k, \mu)$ at each bin follows the Gaussian distribution, where the chi-square χ^2 is calculated in the standard manner from the measured and expected values of $P(k, \mu)$ and its standard deviation.

In reality, however, $P(k, \mu)$ does not follow the Gaussian but the chi-squared distribution because it is calculated as squared of Gaussian-distributed density perturbation [60]. In order to take into account this statistical property in the maximum likelihood estimation, We apply the Wilson-Hilferty (WH) transformation that converts a χ^2 distribution into an approximate Gaussian [67]. We define a new variable

$$P'_{\text{sim}} = (P_{\text{sim}} + P_{\text{shot}})^{1/3}, \quad (4.7)$$

and P'_{sim} is expected to approximately obey the Gaussian distribution with a mean of

$$P'_{\text{true}} = \left[1 - \frac{1}{9N_{\text{mode}}} \right] (P_{\text{true}} + P_{\text{shot}})^{1/3} \quad (4.8)$$

and a variance of

$$\sigma_{P'}^2 = \frac{1}{9N_{\text{mode}}} (P_{\text{true}} + P_{\text{shot}})^{2/3}. \quad (4.9)$$

It should be noted that the power spectrum amplitude directly measured from the simulations, $P_{\text{sim}} + P_{\text{shot}}$, does not exactly obey the chi-squared distribution, because it contains the shot noise term. However, the WH transformation should be effective only at low- k where the number of modes in a (k, μ) bin is small, and the shot noise term is relatively unimportant also at small wavenumbers. Therefore we adopt the above transformation, expecting that $P_{\text{sim}} + P_{\text{shot}}$ approximately obeys a chi-squared distribution. (For the wavenumbers where the shot noise term becomes comparable with the real-space halo power spectrum, see Fig. 4.7.)

After this transformation, we expect that

$$\chi^2 = \sum_{k < k_{\max}} \sum_{\mu} \frac{[P'_{\text{sim}}(k, \mu) - P'_{\text{model}}(k, \mu)]^2}{\sigma_{P', \text{model}}^2} \quad (4.10)$$

approximately obeys a chi-squared distribution, with better accuracy than simply using P_{sim} , where k_{\max} is the upper bound of the range of wavenumbers that we use in fitting, P'_{model} and $\sigma_{P', \text{model}}$ are the WH-transformed model power spectrum and its variance given by eqs. (4.8) and (4.9) with replacing P_{true} by the model power spectrum P_{model} . In our analyses, we vary k_{\max} from 0.05 to 0.50 $h\text{Mpc}^{-1}$ at an interval of 0.05 $h\text{Mpc}^{-1}$.

To see how much the fit is improved by this WH approximation, we will later compare the results with those obtained using the standard chi-square statistic calculation without the WH transformation, in which we simply use P_{sim} , P_{model} and a variance of $\sigma_P^2 = (P_{\text{model}} + P_{\text{shot}})^2 / N_{\text{mode}}$ [62].

4.2 linear growth parameter measurement results

4.2.1 matter power spectrum

Before presenting main results using haloes in the next subsection (4.2.2), let me discuss the robustness of the $f\sigma_8$ measurement for the 2D matter power spectrum. In this subsection, I fixed the bias parameters as $b_0=1$, and $Q=A=0$ in the fitting analysis.

In the upper panel of Fig. 4.1, we show the matter power spectra in real space at $z=2$, 1.35 and 0.5 from bottom to top, respectively. Three arrows indicate $k_{1\%}$ wavenumber defined as

$$\frac{k_{1\%}^2}{6\pi^2} \int_0^{k_{1\%}} dq P_{\text{lin}}(q; z) = C \quad (4.11)$$

with $C = 0.7$, up to which the closure theory is expected to be accurate within 1 per cent level [55, 37]. Actually, we confirmed that the measured power spectra and $P_{\delta\delta}$ predicted by the closure theory at $k_{1\%}$ agree within ~ 3 per cent level. A few per cent deviation arising here may be because of difference in simulation resolution and I think they are still roughly agreement of the definition of $k_{1\%}$. Therefore we use $k_{1\%}$ as indicators of a few per cent accuracy wavenumbers through the paper.

In the lower panel, I show measured $f\sigma_8$ values normalized by the correct ones assumed in simulations ($(f\sigma_8)_{\text{input}} = 0.33, 0.39$ and 0.46 at $z = 2, 1.35$ and 0.5 , respectively), and earned reduced chi-squared values χ_{red}^2 for the best-fitting parameter set. We can find that $f\sigma_8$ from the Kaiser model (open symbols) is significantly underestimated at $k_{\text{max}} \gtrsim 0.10 h\text{Mpc}^{-1}$ at all the redshifts. On the other hand the TNS model (filled symbols) gives $f\sigma_8$ close to the correct one, with systematic errors of less than 4 per cent up to $k_{\text{max}} \sim 0.30 h\text{Mpc}^{-1}$.

As wavenumber increases, χ_{red}^2 boosts up quickly away from unity, and the maximum wavenumber k_{max} up to which $\chi_{\text{red}} \simeq 1$ roughly coincides with $k_{1\%}$. From the TNS model, there are systematic overestimates are seen at $k_{\text{max}} = 0.20$ and $0.25 h\text{Mpc}^{-1}$ at $z = 0.5$. There also are underestimates at $k_{\text{max}} > 0.15 h\text{Mpc}^{-1}$ at $z = 2$. The origin of these systematics is rather uncertain. It can be thought that these might arise from sub-percent uncertainty of the power spectrum prediction by the closure theory, or from the incompleteness in the RSD modeling of the TNS model. However main interest in this theses is in halo power spectra, we will leave these problems for future study.

I get these results through MCMC analysis for the *averaged* power spectrum, P_{ave40} . Thus, the number of modes in each of the (k, μ) bins is rather large compared with that in realistic surveys. We therefore examine whether the correct $f\sigma_8$ could be reconstructed when \hat{P} in eq. (3.1) which is measured from each realisation is used in analysis. Here I will show the fitting results for the power spectrum at $z = 1.35$ with the TNS model in Fig. 4.2. In the figure, filled symbols show the averages of 40 the best-fitting $f\sigma_8$ for each realisation, with and without applying the WH approximation. The measured $f\sigma_8$ are clearly overestimated at small wavenumbers in both cases. I also show the fitting results for the averaged power spectrum with open symbols. Since the overestimating feature is greatly reduced for the results for P_{ave40} that includes a larger number of modes, the systematic overestimation must be caused by the small number of modes in the measured power spectrum. Then we compare the results of filled symbols with and without the WH transformation (magenta triangles and blue circles), and it can be seen that the

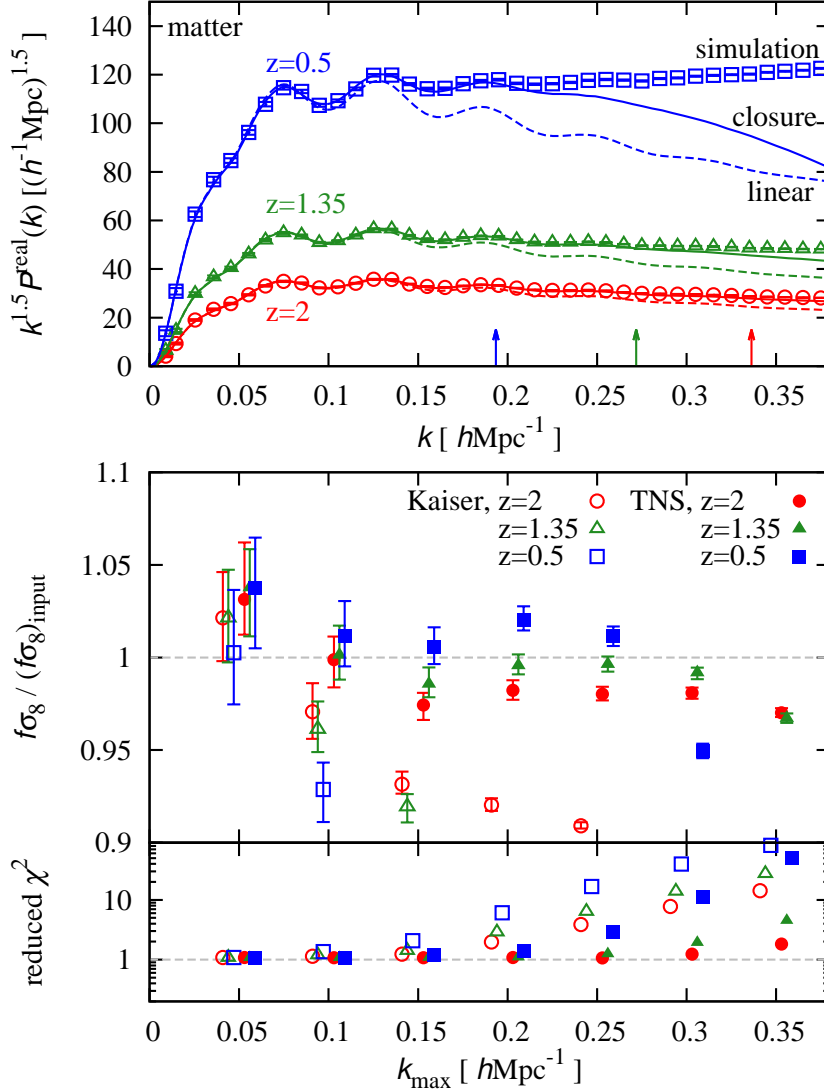


Fig. 4.1. Upper panel: Comparison of the measured matter power spectra from simulations, with the theoretical predictions from the closure theory $P_{\delta\delta}$ (solid lines), and from a linear theory P_{lin} (dashed lines), at the three different redshifts. Arrows indicate the wavenumbers up to which the closure theory is accurate at 1 per cent level ($k_{1\%} = 0.19, 0.27$ and $0.34 h\text{Mpc}^{-1}$ at $z=0.5, 1.35$ and 2 , respectively). Lower panel: The best-fitting $f\sigma_8$ with $1\text{-}\sigma$ error bars and the reduced chi-squared values by fitting with the Kaiser model (open symbols) and with the TNS model (filled symbols) as a function of the maximum wavenumber k_{max} used in fitting. (All the data points are on the same k_{max} grids for the different models and redshifts, but they are slightly shifted horizontally for clarity (see also Fig. 3.1).

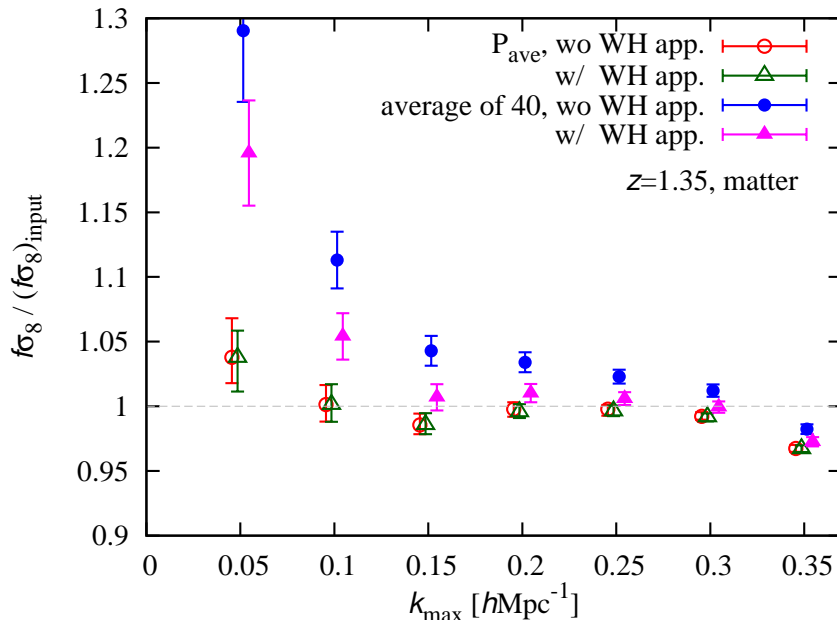


Fig. 4.2. Systematic errors of the $f\sigma_8$ measurements by fitting to the matter power spectrum $P_{\text{matter}}(k, \mu)$ with the TNS model at $z = 1.35$. Open symbols and their error bars show the results from P_{ave40} (averaged power spectrum of 40 realisations) and $1\text{-}\sigma$ statistical errors. Filled symbols show the means of 40 best-fitting $f\sigma_8$ values calculated for each realisation, with the errors estimated by the scatter of the $f\sigma_8$ values of the 40 realisations. Triangles and circles show with and without applying the Wilson-Hilferty approximation, respectively. All the data points are slightly shifted horizontally for clarity (see also Fig. 3.1).

WH transformation improves the accuracy of $f\sigma_8$ estimates. Even after employing the WH transformation, there still remains a discrepancy at $k_{\text{max}} \lesssim 0.10 h\text{Mpc}^{-1}$, which is likely to be the limitation of the WH approximation. However, we think that the WH transformation is useful to get more accurate $f\sigma_8$ estimates than those without it, and always incorporated this technique in MCMC fitting. In the rest of the thesis, we focus on the results of the MCMC analyses after averaging over 40 power spectra, P_{ave40} , with applying the WH transformation to reduce the error induced by a small number of modes in (k, μ) bins.

4.2.2 halo power spectrum

The case of $z = 1.35$ and $M_{\text{min}} = 1.0 \times 10^{12} h^{-1} M_{\odot}$

Then we analysed the halo 2D power spectra and measured $f\sigma_8$ with the four RSD models. As the baseline case, I show the measured $f\sigma_8$ and χ_{red}^2 values from the best-fitting parameters for the halo catalogues of $M_{\text{min}} = 1.0 \times 10^{12} h^{-1} M_{\odot}$ at $z = 1.35$ in Fig. 4.3, as a function of the maximum wavenumber, k_{max} . Here and hereafter, when I present results for a fixed value of k_{max} , I choose the maximum wavenumber $k_{\text{max}} = 0.25 h\text{Mpc}^{-1}$, which is close to $k_{1\%}$ of the closure theory prediction at $z = 1.35$, as the baseline value.

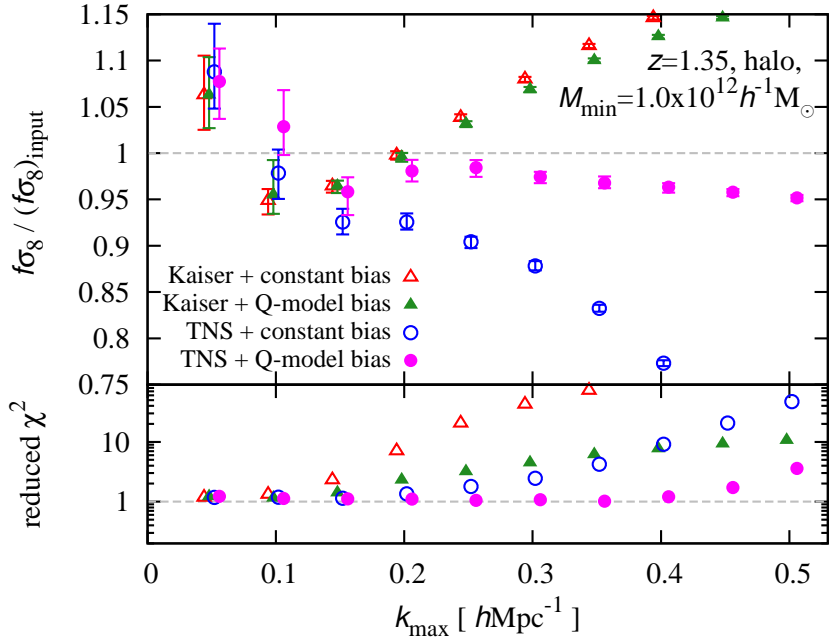


Fig. 4.3. The best-fitting $f\sigma_8$ with $1\text{-}\sigma$ error bars and the reduced chi-squared values, for the halo catalogue of $M_{\min} = 1.0 \times 10^{12} h^{-1} M_{\odot}$ at $z = 1.35$. Data points show the results of the four different models of the 2D halo power spectrum: Kaiser+constant bias, Kaiser+Q-model bias, TNS+constant bias, and TNS+Q-model bias.

All the four models give $f\sigma_8$ within a few per cent accuracy at $k_{\max} \sim 0.10 h\text{Mpc}^{-1}$, up to which linear theory is sufficiently accurate (see dashed lines in the upper panel of Fig. 4.1). There can be seen overestimation by more than $1\text{-}\sigma$ level at $k_{\max} = 0.05 h\text{Mpc}^{-1}$, but these are likely to be cosmic variances. We have checked this as follows: we split the 40 realisations into two groups that contain 20 realisations in each, and measured $f\sigma_8$ for the averaged power spectra of them separately. We confirmed that one of them gives $f\sigma_8$ consistent with the correct value within $1\text{-}\sigma$ level. On the other hand, the underestimation at $k_{\max} = 0.15 h\text{Mpc}^{-1}$ for all the models seem to be systematic errors. It is difficult to identify the causes of these results, since the measured power spectrum can be fitted pretty well with reduced chi-squared values of ~ 1 . I leave this issue for future studies.

Then we investigate the results from the four models one by one. The Kaiser models again fail to reproduce the correct $f\sigma_8$ at $k_{\max} \gtrsim 0.25 h\text{Mpc}^{-1}$, but this time $f\sigma_8$ are overestimated, in contrast to the result for the matter power spectra. Even when the TNS model is employed, the assumption of the constant bias leads to underestimation at $k_{\max} \gtrsim 0.20 h\text{Mpc}^{-1}$. However, when we use the TNS model with the scale-dependent Q-model bias, the systematic error is significantly reduced down to 5 per cent level up to $k_{\max} = 0.50 h\text{Mpc}^{-1}$. Note that the matter power spectrum is accurate with ~ 1 per cent level only up to $k_{\max} = 0.27 h\text{Mpc}^{-1}$. Thus It is rather surprising that the reduced χ^2 values are ~ 1 up to $k_{\max} \sim 0.50 h\text{Mpc}^{-1}$. This means that the parametrization of the Q-model bias can absorb the discrepancy between the matter power spectrum and the closure theory prediction and ~ 5 per cent level systematic errors of $f\sigma_8$ can be achievable

with apparently good fit, which should be kept in mind in future analyses applied on the real data.

We plot in Fig. 4.4 the four best-fitting model power spectra against the simulation data measured at three fixed direction cosine of the wavevector, $\mu = 0.05, 0.55$ and 0.95 . In Fig. 4.5, the halo bias measured from N-body simulations is presented. For the plot of the bias from simulation, I plot the mean of the 40 independently-measured biases in real space as $b(k) = \sqrt{P_{\text{halo}}(k)/P_{\text{m}}(k)}$ from each realisation. Errors on them are $1/\sqrt{40}$ of its standard deviation. For comparison, the best-fitting model bias curves for the four models $b(k)\sigma_8/\sigma_{8,\text{input}}$ are also shown. These curves are calculated for each model with best-fitting values of the corresponding parameters, b_0, Q, A and σ_8 , found in the MCMC chains. The measured bias shows a monotonic increasing trend with the wavenumber. Note that, in general, the scale-dependence of the halo bias is different for different halo mass and redshift, and show both increasing and decreasing trends [68, 29, 38].

When the Kaiser model is used, the apparently inverse trend of the the systematic errors for matter and haloes can be understood as follows. In a fitting to the matter spectrum, the Kaiser model tries to reproduce the power enhancement arising from the non-linear evolution at high- k by setting σ_8 larger than the input value, because of the absence of the bias model parameters (see dash-dotted line at $\mu \sim 0$ in the lower panel of Fig. 4.4). It is easy to show that, from the Kaiser formula, a systematically lower value of $f\sigma_8$ than the input value is favored to reproduce the RSD effect at large μ , when σ_8 is overestimated. In a fitting to the halo spectrum, there are additional degrees of freedom of the bias parametrization, but the non-linear power enhancement at high- k cannot be completely absorbed by the constant or Q-model bias. Thus the power enhancement can also be absorbed to some extent by reducing σ_v in the FoG damping factor, but Fig. 4.6 indicates that the best-fitting σ_v is zero for the Kaiser models. The power enhancement that cannot be absorbed by bias modelings or the FoG parameter favors a larger $f\sigma_8$ than the correct value, at the cost of a poor agreement at low- k .

The systematic underestimation of $f\sigma_8$ when we employ the TNS+constant bias model might be a result of the discrepancy between the correct bias measured directly from simulations and the best-fitting constant bias at low- k ($k \lesssim 0.15 h\text{Mpc}^{-1}$, see dashed line in Fig. 4.5). The bias parameter raised up by the non-linear power enhancement at high- k causes small $f\sigma_8$ value than the correct one and larger σ_v than that from the TNS+Q-model bias model.

For the TNS+Q-model bias, there remains ~ 2 per cent discrepancy in bias reconstruction at $k = 0.25 h\text{Mpc}^{-1}$ which may be due to imperfectness of the RSD modeling. This need to be further investigated in future to pursue more accurate modeling of the 2D halo power spectrum.

In the end of this subsection, I refer about the sizes of statistical errors on measured $f\sigma_8$. Compared with those for the Kaiser+constant bias model, we get nearly equal sizes of errors for the Kaiser+Q-model bias, 1.5–2 times larger errors for the TNS+constant bias and 2.5 times larger errors for the TNS+Q-model bias. The size of statistical error becomes generally larger with increasing the number of fitting model parameters because of the effect of marginalizing, though the size of increase is quantitatively different for different models because of different ways of parameter degeneracy.

Dependence on z and M_{min}

Then we investigate the other halo catalogues at the three redshifts with different minimum halo mass thresholds. The results of the $f\sigma_8$ measurement by fitting with the

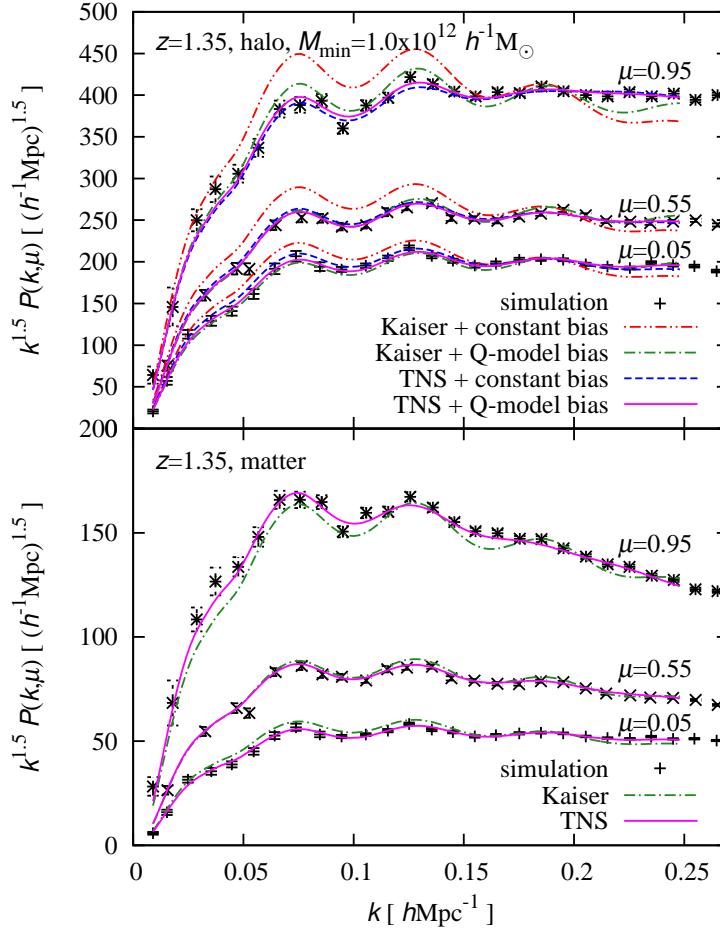


Fig. 4.4. The power spectra in redshift space at $\mu = 0.05, 0.55$ and 0.95 at $z = 1.35$. The upper panel is for the halo catalogue of $M_{\min} = 1.0 \times 10^{12} h^{-1} M_{\odot}$, while the lower panel is for the matter distribution. The data points are measurements from simulations and the curves show the best fits for different models (see labels in the figure for corresponding models).

TNS+Q-model bias are shown in Fig. 4.7. I firstly focus on the results at $k_{\max} \sim k_{1\%}$. In this regime $f\sigma_8$ measurements with systematic uncertainties of less than ~ 5 per cent are achieved, except for massive halo catalogues of $M_{\min} \gtrsim 10^{13} h^{-1} M_{\odot}$ at $z = 2$. These correspond to highly biased haloes of $b_0\sigma_8/\sigma_{8,\text{input}} \gtrsim 4$. Therefore we can state that the TNS+Q-model bias can be used for $f\sigma_8$ measurements with an accuracy of 5 per cent if $k_{\max} \sim k_{1\%}$ for the haloes with $b \lesssim 4$. The results of systematic errors of $f\sigma_8$ are summarized in Table 4.1.

To investigate the causes of systematic errors for massive halo catalogues, I plot the 2D halo power spectrum and measured bias for the halo catalogue with $M_{\min} = 2.0 \times 10^{13} h^{-1} M_{\odot}$ at $z = 2$ with the best-fitting curves from TNS+Q-model bias in Fig. 4.8. In the figure I show the result for $k_{\max} = 0.35 h\text{Mpc}^{-1}$. The power spectrum is well fitted with reduced χ^2 values of 1.6. However, in the lower panel we can see poor fit of

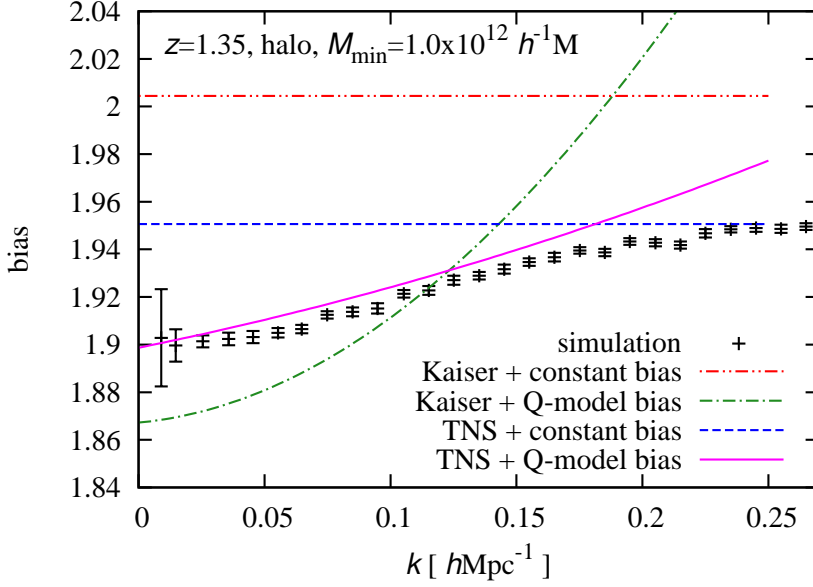


Fig. 4.5. Comparison between the halo bias directly measured from simulations and the best-fitting bias models, for the halo catalog of $M_{\min} = 1.0 \times 10^{12} h^{-1} M_{\odot}$ at $z = 1.35$. The data points and lines are for the same simulation and models as those in the upper panel of Fig. 4.4.

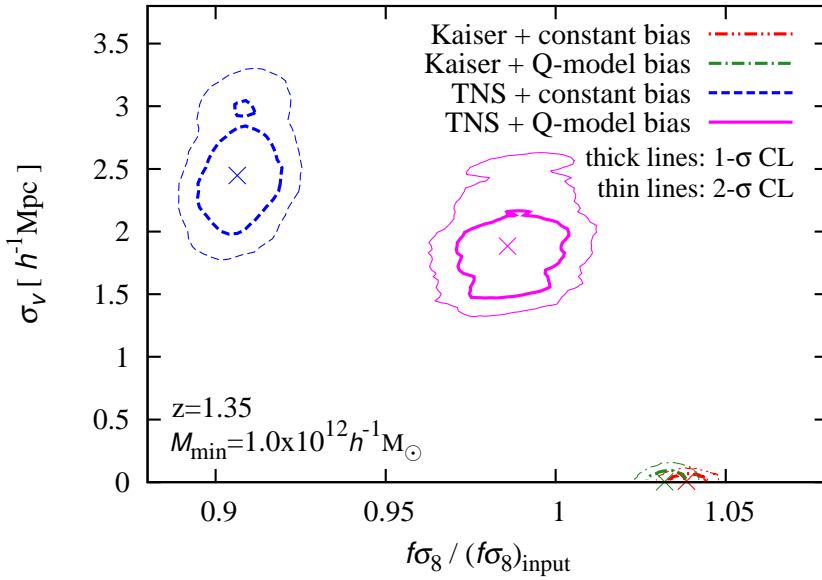


Fig. 4.6. The best-fitting values and the 1- and 2- σ confidence regions of the four different models (see figure) in the $f\sigma_8$ - σ_v plane, for the halo catalogue of $M_{\min} = 1.0 \times 10^{12} h^{-1} M_{\odot}$ at $z = 1.35$.

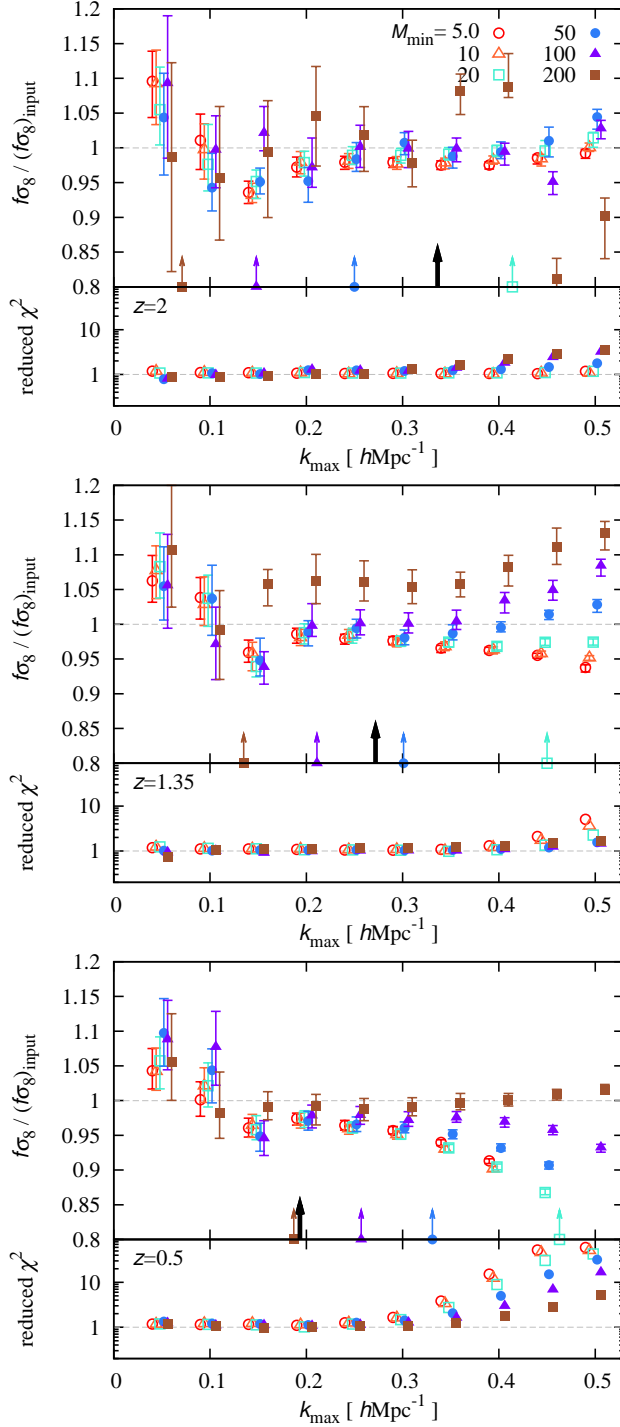


Fig. 4.7. The best-fitting $f\sigma_8$ and the reduced chi-squared values at $z=2, 1.35$ and 0.5 from top to bottom, respectively. Different symbols are for the different values of the minimum halo mass $M_{\text{min}} = 5.0, 10, 20, 50, 100$ and 200 in units of $10^{11} h^{-1} M_{\odot}$. Black arrows show the $k_{1\%}$ wavenumbers. Cyan, blue, purple and brown arrows with symbols indicate the wavenumbers where the shot noise term becomes comparable with the halo power spectrum in real space, for the catalogues of $M_{\text{min}} = 20, 50, 100$ and 200 , respectively

Table 4.1. Summary of the systematic errors of $f\sigma_8$ measurements from the TNS+Q-model bias model fitting. M_{\min} , $\overline{M}_{\text{halo}}$ and bias are the same as those in Table 3.1, and systematic error columns show $f\sigma_8/(f\sigma_8)_{\text{input}} - 1$ when we use the wavenumber range up to $k_{\max} \sim k_{1\%}$ (namely, $k_{\max} = 0.35, 0.25$ and $0.20 h\text{Mpc}^{-1}$ at $z = 2, 1.35$ and 0.5 , respectively) in fitting analysis. For clarity, halo catalogues with systematic errors over 5% are written in red letter.

M_{\min}	$\overline{M}_{\text{halo}}$	$z=2$		$z=1.35$			$z=0.5$		
		bias	sys. error	$\overline{M}_{\text{halo}}$	bias	sys. error	$\overline{M}_{\text{halo}}$	bias	sys. error
5.0×10^{11}	1.51×10^{12}	2.3	-2.5%	1.92×10^{12}	1.7	-2.1%	2.83×10^{12}	1.1	-2.6%
1.0×10^{12}	2.65×10^{12}	2.6	-2.2%	3.32×10^{12}	1.9	-1.6%	4.90×10^{12}	1.2	-3.1%
2.0×10^{12}	4.61×10^{12}	3.1	-0.9%	5.71×10^{12}	2.2	-1.6%	8.36×10^{12}	1.4	-2.4%
5.0×10^{12}	9.80×10^{12}	3.9	-1.2%	1.19×10^{13}	2.7	-0.6%	1.70×10^{13}	1.7	-2.9%
1.0×10^{13}	1.74×10^{13}	4.7	-0.1%	2.08×10^{13}	3.3	+0.1%	2.90×10^{13}	1.9	-2.1%
2.0×10^{13}	3.13×10^{13}	6.1	+8.2%	3.66×10^{13}	4.0	+6.1%	4.96×10^{13}	2.3	-0.8%

the reconstructed bias curve to the measured bias. The singularity in the curve at $k = 0.27 h\text{Mpc}^{-1}$ is due to the negative best-fitting value of bias parameter A . For comparison I also fitted Q-model bias directly to the measured bias and got almost the same best-fitting curve with the reconstructed one, suggesting that the strong scale-dependence of the halo bias for the heavy haloes is hard to be fit with the Q-model bias, and deviation of from the correct bias may propagate and cause the systematic error in $f\sigma_8$ measurement. In addition, the assumption in the TNS+Q-model bias formulation that the scale dependence of the bias is small should be broken for this case.

The behavior beyond $k_{1\%}$ depends on the mass of haloes as well as redshift. In some cases, a value of $f\sigma_8$ consistent with its input value is successfully recovered up to much higher wavenumbers (see e.g., the heaviest halo catalogue at $z = 0.5$, from which we can measure the correct $f\sigma_8$ values up to $k_{\max} = 0.45 h\text{Mpc}^{-1}$). However this result should be taken with care. This apparently successful recovery of $f\sigma_8$ is probably because of the rather flexible functional form of the scale-dependent bias adopted in the analysis. The parameters A and Q can sometimes absorb the mismatch between the true *matter* power spectra and the TNS model beyond $k_{1\%}$ without leaving systematics to $f\sigma_8$ for some special cases. The situation would probably be quite different when different parameterizations are chosen for $b(k)$. Nevertheless, it is of interest to explore the possibility to add some more information from higher wavenumbers. Although we, in this paper, employ only one particular functional form for the scale-dependent bias as well as a constant bias model, the reproductivity of the growth-rate parameter from high- k modes with different bias functions is also of interest. We leave further investigations along this line for future studies.

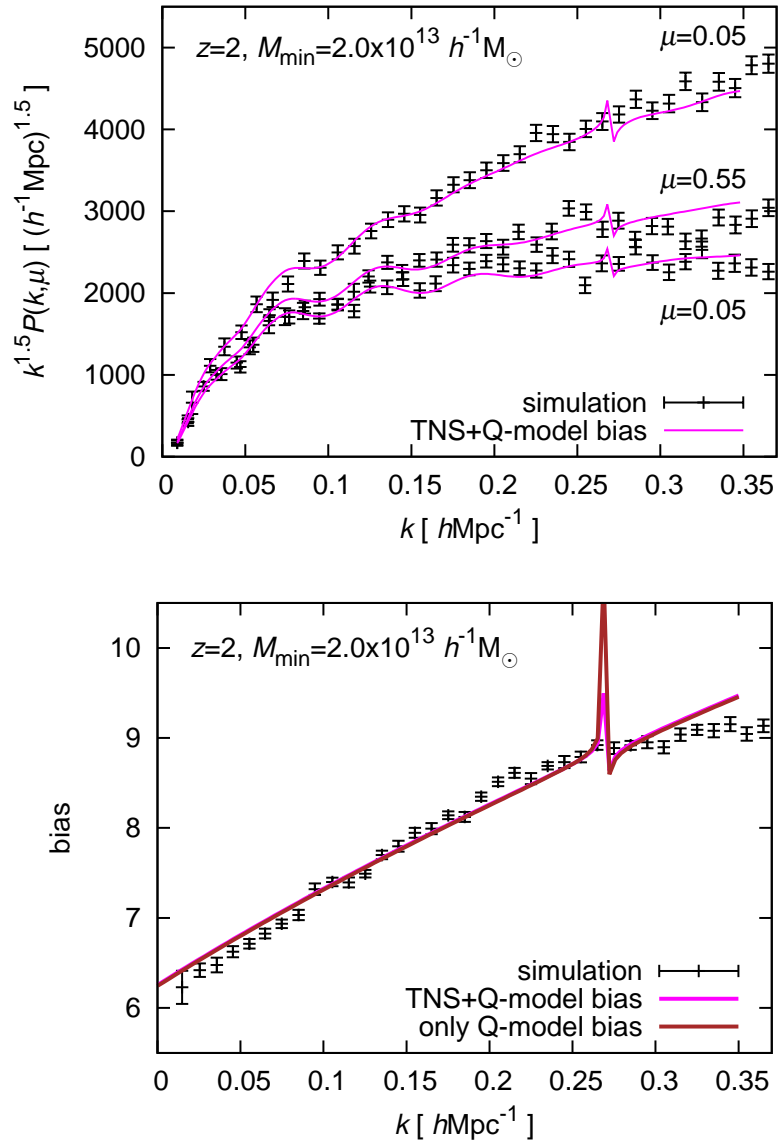


Fig. 4.8. Upper panel: The 2D halo power spectrum for $M_{\min} = 2.0 \times 10^{13} h^{-1} M_{\odot}$ halo catalogue at $z=2$. The spectrum at three direction cosine values, $\mu=0.05$, 0.55 and 0.95 , are plotted from bottom to top, respectively. Magenta line shows the best-fitting curve fit with the TNS+Q-model bias. Lower panel: Measured bias for the same catalogue. Magenta line shows the reconstructed bias curve using bias parameters in the best-fitting parameter set by fitting TNS+Q-model bias to the halo power spectrum, whereas brown one shows the best-fitting curve fit with Q-model bias directly.

4.3 Implications for Future Surveys

In this section, we give some implications for future analysis for coming redshift surveys with large statistics. As seen above, we have demonstrated that we can measure $f\sigma_8$ with a systematic error of $\lesssim 5$ per cent by employing the TNS+Q-model bias, up to the wavenumber range $k_{\max} \sim k_{1\%}$ for not strongly biased haloes (i.e., haloes with $b \lesssim 4$).

Some of expected constraints on the growth rate $f(z)$ for some on-going and planned surveys are presented in [38] and they are, at 1- σ level, 7.5–3.9 per cent at redshift $z=0.7$ –1.5 for SuMIRe-PFS, and 5.1 per cent at $z=3.0$ for HETDEX. Expecting that f and $f\sigma_8$ are constrained at the same level, the TNS+Q-model bias achieves lower than or comparable level systematic error compared to the expected statistical errors from these surveys.

The space mission *Euclid* will survey over a redshift range of $0.7 < z < 2.1$ and get redshifts of 50 million galaxies. The number of galaxies in each redshift bin will be more than one million. Using following empirical estimator for statistical errors,

$$\frac{\Delta(f\sigma_8)}{f\sigma_8} \sim \frac{50}{\sqrt{N_{\text{gal}}}} \quad (4.12)$$

where N_{gal} is the number of galaxies [19, 69], we can roughly estimate the statistical error expected from *Euclid* to be a few per cent level, indicating that we need to further improve the modeling of RSD in Euclid era.

Chapter 5

Summary and Conclusion

In this thesis, I investigate the systematic errors on the measurement of linear growth parameter, $f\sigma_8$, using RSD. I generated various halo catalogues by using N-body simulations, and analysed by fitting some RSD models to the measured 2D halo power spectrum. I summarize the thesis below.

In chapter 2, I firstly review the evolution of the universe and of the density fluctuations, and explain how RSD effects arise. Then I derive the Kaiser formula for the 2D power spectrum in linear theory and introduce a recently-developed non-linear model, the TNS model, which including higher-order mode coupling correction terms. I also explain the treatment of the galaxy (or halo) bias to be incorporated into these models.

I describe the settings of N-body simulation that we have carried out, and the measurement of the power spectra for the generated halo catalogues in chapter 3. I used public code `Gadget2` in the simulations with employing 1024^3 DM particles in a cubic box with length of $700h^{-1}\text{Mpc}$, which gives the mass resolution of $2.4 \times 10^{10} h^{-1}M_\odot$. The initial power spectrum was calculated at $z_{\text{ini}} = 49$ by `CAMB` and snapshots were dumped at the three redshifts, $z = 2, 1.35$ and 0.5 . By using FoF algorithm, I identified haloes from the simulations and generated various catalogues with different math thresholds (For details of the catalogues, please see Table. 3.1).

In the section 4.1, I review the RSD models that we tested in this thesis with the searched parameters in the models. MCMC technique and the Wilson-Hilferty approximation employed in the fitting analysis are also explained here. The tested RSD models in this thesis are the combination of two types of RSD modeling as

$$P(k, \mu) = \begin{cases} D_{\text{FoG}}(k\mu f\sigma_v) \times b^2(1 + \beta\mu^2)^2 P_{\text{lin}}(k) & \text{: the Kaiser model} \\ D_{\text{FoG}}(k\mu f\sigma_v) \times b^2 \left[P_{\delta\delta}(k) + 2\beta\mu^2 P_{\delta\theta}(k) + \beta^2\mu^4 P_{\theta\theta}(k) \right. \\ \qquad \qquad \qquad \left. + bC_A(k, \mu; \beta) + b^2C_B(k, \mu; \beta) \right] & \text{: the TNS model} \end{cases}$$

with two types of bias parametrizations as

$$b(k) = \begin{cases} b_0 & \text{: constant bias} \\ b_0 \sqrt{\frac{1 + Qk^2}{1 + Ak}} & \text{: Q-model bias} \end{cases} .$$

Section 4.2 shows the results of our analysis. For the halo catalogues of $M_{\text{min}} = 1.0 \times 10^{11} h^{-1}M_\odot$ at $z = 1.35$, all the four models give $f\sigma_8$ within a few per cent accuracy at $k_{\text{max}} \sim 0.10 h\text{Mpc}^{-1}$, up to which linear theory is sufficiently accurate. At $k_{\text{max}} \gtrsim 0.25 h\text{Mpc}^{-1}$ up to which the matter power spectrum prediction from the closure theory

is expected to be accurate at ~ 1 per cent level, the Kaiser models overestimate $f\sigma_8$ compared with the correct one. Also the TNS+constant bias fails to reproduce the correct value, but in this case this model underestimates $f\sigma_8$ in contrast to the Kaiser models. By taking a closer look at the reconstructed model power spectra and biases, I clarify the causes of these over- and underestimation trends. When we use the TNS model with the scale-dependent Q-model bias, the systematic error is significantly reduced down to < 5 per cent level, surprisingly, up to $k_{\max} = 0.50 h\text{Mpc}^{-1}$. This would mean that the parametrization of the Q-model bias can absorb the discrepancy between the matter power spectrum and the closure theory prediction to some extent, which should be kept in mind in future analyses. Furthermore, from the analysis of the other halo catalogues, I demonstrate that the TNS model with Q-model bias can be used for $f\sigma_8$ measurements within an accuracy of 5 per cent if $k_{\max} \sim k_{1\%}$ for the haloes with $b \lesssim 4$.

Our RSD model, as stated in section 4.3, achieves lower than or comparable level systematic error compared to the expected statistical errors from future ground-base surveys, such as SuMIRe-PFS and HETDEX. However in the Euclid era, about 50 million of redshifts of galaxies will be measured by satellite observation will give at a few per cent level constraint on the linear growth parameter measurement. We need to make further efforts to improve the modeling of RSD by that era to make the best out of the observation data and reveal the nature of dark energy even in the slightest bit.

Acknowledgement

It is a great pressure to thank my supervisor, prof. Totani in Univ. Tokyo, for all of my study life in the graduate school not only for giving me the highly amusing theme of RSD but also always advising me to promote this research. I also thank all of my collaborators. Assistant prof. Takahashi in Hirosaki Univ. taught me from A to Z of N-body simulation and measuring the power spectrum. Dr. Nishimichi in Institut d'Astrophysique de Paris, from whom I learned MCMC and the WH approximation technique, always helps me when I have difficulties in the analysis. Prof. Yoshida in the Kavli Institute for the Physics and Mathematics of the Universe at Univ. Tokyo, who is as known as one of the developers of `Gadget2` code, gave me advices kindly and led me the direction of what to investigate next with the view of future cosmological studies. Assoc. prof. Taruya in Yukawa Institute for Theoretical Physics served me with the templates of the power spectrum based on which we proceed the analysis, and told me a lot about state-of-art w themes in observational cosmology study. In addition, I often discuss over a wide range of subjects on observational cosmology with Sumiyoshi-san, Tonegawa-san and Okada-san as co-workers in the same laboratory. Since they works mainly in observational side of FastSound team, the discussion help me to better generate halo catalogues in my simulations. Discussion with these people is always very interesting and has motivated me.

I feel very fortunate to belong to the theoretical group in the department of Astronomy, in which there are many staffs and students study *not* in cosmology. From interdisciplinary discussion with them I have learnt various techniques of simulations and analysis methodologies. Especially, I thank prof. Mineshige for both of research and mental supports.

In addition to the above, I thank many friends in Yoshida student dormitory. Since they are in various major fields, e.g., mathematics, mathematical biology, medicine and informatics, they gives me a great amount of comments of statistics and about effective programing techniques from time to time. Lastly, Ribbon and Fukinoto, which are gouts parent and the child we have in the dormitory, I have been soothed through taking care of them every day.

Bibliography

- [1] Adam G. Riess, Alexei V. Filippenko, Peter Challis, Alejandro Clocchiatti, Alan Diercks, Peter M. Garnavich, Ron L. Gilliland, Craig J. Hogan, Saurabh Jha, Robert P. Kirshner, B. Leibundgut, M. M. Phillips, David Reiss, Brian P. Schmidt, Robert A. Schommer, R. Chris Smith, J. Spyromilio, Christopher Stubbs, Nicholas B. Suntzeff, and John Tonry. Observational Evidence from Supernovae for an Accelerating Universe and a Cosmological Constant. *The Astronomical Journal*, 116(3):1009–1038, September 1998.
- [2] S. Perlmutter, G. Aldering, G. Goldhaber, R. A. Knop, P. Nugent, P. G. Castro, S. Deustua, S. Fabbro, A. Goobar, D. E. Groom, I. M. Hook, A. G. Kim, M. Y. Kim, J. C. Lee, N. J. Nunes, R. Pain, C. R. Pennypacker, R. Quimby, C. Lidman, R. S. Ellis, M. Irwin, R. G. McMahon, P. Ruiz - Lapuente, N. Walton, B. Schaefer, B. J. Boyle, A. V. Filippenko, T. Matheson, A. S. Fruchter, N. Panagia, H. J. M. Newberg, W. J. Couch, and The Supernova Cosmology Project. Measurements of Ω and Λ from 42 High - Redshift Supernovae. *The Astrophysical Journal*, 517(2):565–586, June 1999.
- [3] D. N. Spergel, L Verde, H. V. Peiris, E. Komatsu, M. R. Nolta, C. L. Bennett, M. Halpern, G. Hinshaw, N. Jarosik, A. Kogut, M. Limon, S. S. Meyer, L. Page, G. S. Tucker, J. L. Weiland, E. Wollack, and E. L. Wright. First Year Wilkinson Microwave Anisotropy Probe (WMAP) Observations: Determination of Cosmological Parameters. *The Astrophysical Journal*, page 51, 2003.
- [4] Max Tegmark, Michael Strauss, Michael Blanton, Kevork Abazajian, Scott Dodelson, Havard Sandvik, Xiaomin Wang, David Weinberg, Idit Zehavi, Neta Bahcall, Fiona Hoyle, David Schlegel, Roman Scoccimarro, Michael Vogeley, Andreas Berlind, Tamás Budavari, Andrew Connolly, Daniel Eisenstein, Douglas Finkbeiner, Joshua Frieman, James Gunn, Lam Hui, Bhuvnesh Jain, David Johnston, Stephen Kent, Huan Lin, Reiko Nakajima, Robert Nichol, Jeremiah Ostriker, Adrian Pope, Ryan Scranton, Uroš Seljak, Ravi Sheth, Albert Stebbins, Alexander Szalay, István Szapudi, Yongzhong Xu, James Annis, J. Brinkmann, Scott Burles, Francisco Castander, Istvan Csabai, Jon Loveday, Mamoru Doi, Masataka Fukugita, Bruce Gillespie, Greg Hennessy, David Hogg, Željko Ivezić, Gillian Knapp, Don Lamb, Brian Lee, Robert Lupton, Timothy McKay, Peter Kunszt, Jeffrey Munn, Liam O’Connell, John Peoples, Jeffrey Pier, Michael Richmond, Constance Rockosi, Donald Schneider, Christopher Stoughton, Douglas Tucker, Daniel Vanden Berk, Brian Yanny, and Donald York. Cosmological parameters from SDSS and WMAP. *Physical Review D*, 69(10):103501, May 2004.
- [5] Alan H. Guth. Inflationary universe: A possible solution to the horizon and flatness problems. *Physical Review D*, 23(2):347–356, January 1981.
- [6] P. A. R. Ade, N. Aghanim, C. Armitage-Caplan, M. Arnaud, M. Ashdown, F. Atrio-Barandela, J. Aumont, C. Baccigalupi, A. J. Banday, R. B. Barreiro, J. G. Bartlett,

- E. Battaner, K. Benabed, A. Benoît, A. Benoit-Lévy, J.-P. Bernard, M. Bersanelli, P. Bielewicz, J. Bobin, J. J. Bock, A. Bonaldi, J. R. Bond, J. Borrill, F. R. Bouchet, M. Bridges, M. Bucher, C. Burigana, R. C. Butler, E. Calabrese, B. Cappellini, J.-F. Cardoso, A. Catalano, A. Challinor, A. Chamballu, R.-R. Chary, X. Chen, H. C. Chiang, L.-Y. Chiang, P. R. Christensen, S. Church, D. L. Clements, S. Colombi, L. P. L. Colombo, F. Couchot, A. Coulais, B. P. Crill, A. Curto, F. Cuttaia, L. Danese, R. D. Davies, R. J. Davis, P. de Bernardis, A. de Rosa, G. de Zotti, J. Delabrouille, J.-M. Delouis, F.-X. Désert, C. Dickinson, J. M. Diego, K. Dolag, H. Dole, S. Donzelli, O. Doré, M. Douspis, J. Dunkley, X. Dupac, G. Efstathiou, F. Elsner, T. A. Enßlin, H. K. Eriksen, F. Finelli, O. Forni, M. Frailis, A. A. Fraisse, E. Franceschi, T. C. Gaier, S. Galeotta, S. Galli, K. Ganga, M. Giard, G. Giardino, Y. Giraud-Héraud, E. Gjerløw, J. González-Nuevo, K. M. Górski, S. Gratton, A. Gregorio, A. Gruppuso, J. E. Gudmundsson, J. Haissinski, J. Hamann, F. K. Hansen, D. Hanson, D. Harrison, S. Henrot-Versillé, C. Hernández-Monteagudo, D. Herranz, S. R. Hildebrandt, E. Hivon, M. Hobson, W. A. Holmes, A. Hornstrup, Z. Hou, W. Hovest, K. M. Huffmanberger, A. H. Jaffe, T. R. Jaffe, J. Jewell, W. C. Jones, M. Juvela, E. Keihänen, R. Kesitalo, T. S. Kisner, R. Kneissl, J. Knoche, L. Knox, M. Kunz, H. Kurki-Suonio, G. Lagache, A. Lähteenmäki, J.-M. Lamarre, A. Lasenby, M. Lattanzi, R. J. Laureijs, C. R. Lawrence, S. Leach, J. P. Leahy, R. Leonardi, J. León-Tavares, J. Lesgourgues, A. Lewis, M. Liguori, P. B. Lilje, M. Linden-Vørnle, M. López-Cañiego, P. M. Lubin, J. F. Macías-Pérez, B. Maffei, D. Maino, N. Mandolesi, M. Maris, D. J. Marshall, P. G. Martin, E. Martínez-González, S. Masi, M. Massardi, S. Matarrese, F. Matthai, P. Mazzotta, P. R. Meinhold, A. Melchiorri, J.-B. Melin, L. Mendes, E. Menegoni, A. Mennella, M. Migliaccio, M. Millea, S. Mitra, M.-A. Miville-Deschênes, A. Moneti, L. Montier, G. Morgante, D. Mortlock, A. Moss, D. Munshi, J. A. Murphy, P. Naselsky, F. Nati, P. Natoli, C. B. Netterfield, H. U. Nørgaard Nielsen, F. Novello, D. Novikov, I. Novikov, I. J. O’Dwyer, S. Osborne, C. A. Oxborrow, F. Paci, L. Pagano, F. Pajot, R. Paladini, D. Paoletti, B. Partridge, F. Pasian, G. Patanchon, D. Pearson, T. J. Pearson, H. V. Peiris, O. Perdereau, L. Perotto, F. Perrotta, V. Pettorino, F. Piacentini, M. Piat, E. Pierpaoli, D. Pietrobon, S. Plaszczynski, P. Platania, E. Pointecouteau, G. Polenta, N. Ponthieu, L. Popa, T. Poutanen, G. W. Pratt, G. Prézeau, S. Prunet, J.-L. Puget, J. P. Rachen, W. T. Reach, R. Rebolo, M. Reinecke, M. Remazeilles, C. Renault, S. Ricciardi, T. Riller, I. Ristorcelli, G. Rocha, C. Rosset, G. Roudier, M. Rowan-Robinson, J. A. Rubiño Martín, B. Rusholme, M. Sandri, D. Santos, M. Savelainen, G. Savini, D. Scott, M. D. Seiffert, E. P. S. Shellard, L. D. Spencer, J.-L. Starck, V. Stolyarov, R. Stompor, R. Sudiwala, R. Sunyaev, F. Sureau, D. Sutton, A.-S. Suur-Uski, J.-F. Sygnet, J. A. Tauber, D. Tavagnacco, L. Terenzi, L. Toffolatti, M. Tomasi, M. Tristram, M. Tucci, J. Tuovinen, M. Türler, G. Umata, L. Valenziano, J. Valiviita, B. Van Tent, P. Vielva, F. Villa, N. Vittorio, L. A. Wade, B. D. Wandelt, I. K. Wehus, M. White, S. D. M. White, A. Wilkinson, D. Yvon, A. Zacchei, and A. Zonca. Planck 2013 results. XVI. Cosmological parameters. *Astronomy & Astrophysics*, 571:A16, October 2014.
- [7] Yong-Seon Song, Wayne Hu, and Ignacy Sawicki. Large scale structure of $f(R)$ gravity. *Physical Review D*, 75(4):044004, February 2007.
- [8] Gia Dvali, Gregory Gabadadze, and Massimo Porrati. 4D gravity on a brane in 5D Minkowski space. *Physics Letters B*, 485(1-3):208–214, July 2000.
- [9] Alberto Nicolis, Riccardo Rattazzi, and Enrico Trincherini. Galileon as a local modification of gravity. *Physical Review D*, 79(6):064036, March 2009.

- [10] D. J. Eisenstein, I Zehavi, D. W. Hogg, R. Scoccimarro, M. R. Blanton, R. C. Nichol, R. Scranton, H. Seo, M. Tegmark, Z. Zheng, S. Anderson, J. Annis, N. Bahcall, J. Brinkmann, S. Burles, F. J. Castander, A. Connolly, I. Csabai, M. Doi, M. Fukugita, J. A. Frieman, K. Glazebrook, J. E. Gunn, J. S. Hendry, G. Hennessy, Z. Ivezić, S. Kent, G. R. Knapp, H. Lin, Y. Loh, R. H. Lupton, B. Margon, T. McKay, A. Meiksin, J. A. Munn, A. Pope, M. Richmond, D. Schlegel, D. Schneider, K. Shimasaku, C. Stoughton, M. Strauss, M. SubbaRao, A. S. Szalay, I. Szapudi, D. Tucker, B. Yanny, and D. York. Detection of the Baryon Acoustic Peak in the Large-Scale Correlation Function of SDSS Luminous Red Galaxies. *The Astrophysical . . .*, pages 560–574, 2005.
- [11] Nick Kaiser. Clustering in real space and in redshift space. *Monthly Notices of the Royal Astronomical Society*, 227:1–21, July 1987.
- [12] J. C. Jackson. A Critique of Rees’s Theory of Primordial Gravitational Radiation. *Monthly Notices of the Royal Astronomical Society*, 156(1):1P–5P, February 1972.
- [13] J. R. Tully, R. B.; Fisher. Nearby small groups of galaxies. *MNRAS*, 1978.
- [14] A. J. S. Hamilton. Linear Redshift Distortions: a Review. In D Hamilton, editor, *The Evolving Universe*, volume 231 of *Astrophysics and Space Science Library*, page 185, 1998.
- [15] H. Tadros, W. E. Ballinger, A. N. Taylor, A. F. Heavens, G. Efstathiou, W. Saunders, C. S. Frenk, O. Keeble, R. McMahon, S. J. Maddox, S. Oliver, M. Rowan-Robinson, W. J. Sutherland, and S. D. M. White. Spherical harmonic analysis of the PSCz galaxy catalogue: redshift distortions and the real-space power spectrum. *Monthly Notices of the Royal Astronomical Society*, 305(3):527–546, May 1999.
- [16] Will J. Percival, Daniel Burkey, Alan Heavens, Andy Taylor, Shaun Cole, John A. Peacock, Carlton M. Baugh, Joss Bland-Hawthorn, Terry Bridges, Russell Cannon, Matthew Colless, Chris Collins, Warrick Couch, Gavin Dalton, Roberto De Propriis, Simon P. Driver, George Efstathiou, Richard S. Ellis, Carlos S. Frenk, Karl Glazebrook, Carole Jackson, Ofer Lahav, Ian Lewis, Stuart Lumsden, Steve Maddox, Peder Norberg, Bruce A. Peterson, Will Sutherland, and Keith Taylor. The 2dF Galaxy Redshift Survey: spherical harmonics analysis of fluctuations in the final catalogue. *Monthly Notices of the Royal Astronomical Society*, 353(4):1201–1218, October 2004.
- [17] Shaun Cole, Will J Percival, John A Peacock, Peder Norberg, Carlton M. Baugh, Carlos S Frenk, Ivan Baldry, Joss Bland-Hawthorn, Terry Bridges, Russell Cannon, Matthew Colless, Chris Collins, Warrick Couch, Nicholas J. G. Cross, Gavin Dalton, Vincent R Eke, Roberto De Propriis, Simon P. Driver, George Efstathiou, Richard S Ellis, Karl Glazebrook, Carole Jackson, Adrian Jenkins, Ofer Lahav, Ian Lewis, Stuart Lumsden, Steve Maddox, Darren Madgwick, Bruce A Peterson, Will Sutherland, and Keith Taylor. The 2dF Galaxy Redshift Survey: power-spectrum analysis of the final data set and cosmological implications. *Monthly Notices of the Royal Astronomical Society*, 362(2):505–534, September 2005.
- [18] Florian Beutler, Chris Blake, Matthew Colless, D. Heath Jones, Lister Staveley-Smith, Gregory B. Poole, Lachlan Campbell, Quentin Parker, Will Saunders, and Fred Watson. The 6dF Galaxy Survey: $z = 0$ measurements of the growth rate and σ_8 . *Monthly Notices of the Royal Astronomical Society*, 423(4):3430–3444, July 2012.
- [19] L Guzzo, M Pierleoni, B Meneux, E Branchini, O Le Fèvre, C Marinoni, B Garilli, J Blaizot, G De Lucia, A Pollo, H J McCracken, D Bottini, V Le Brun, D Maccagni, J P Picat, R Scaramella, M Scodreggio, L Tresse, G Vettolani, A Zanichelli, C Adami, S Arnouts, S Bardelli, M Bolzonella, A Bongiorno, A Cappi, S Charlot, P Ciliegi,

- T Contini, O Cucciati, S de la Torre, K Dolag, S Foucaud, P Franzetti, I Gavignaud, O Ilbert, A Iovino, F Lamareille, B Marano, A Mazure, P Memeo, R Merighi, L Moscardini, S Paltani, R Pellò, E Perez-Montero, L Pozzetti, M Radovich, D Vergani, G Zamorani, and E Zucca. A test of the nature of cosmic acceleration using galaxy redshift distortions. *Nature*, 451(7178):541–4, January 2008.
- [20] Chris Blake, Sarah Brough, Matthew Colless, Carlos Contreras, Warrick Couch, Scott Croom, Tamara Davis, Michael J. Drinkwater, Karl Forster, David Gilbank, Mike Gladders, Karl Glazebrook, Ben Jelliffe, Russell J. Jurek, I-hui Li, Barry Madore, D. Christopher Martin, Kevin Pimblet, Gregory B. Poole, Michael Pracy, Rob Sharp, Emily Wisnioski, David Woods, Ted K. Wyder, and H. K. C. Yee. The WiggleZ Dark Energy Survey: the growth rate of cosmic structure since redshift $z=0.9$. *Monthly Notices of the Royal Astronomical Society*, 415(3):2876–2891, August 2011.
- [21] Carlos Contreras, Chris Blake, Gregory B. Poole, Felipe Marin, Sarah Brough, Matthew Colless, Warrick Couch, Scott Croom, Darren Croton, Tamara M. Davis, Michael J. Drinkwater, Karl Forster, David Gilbank, Mike Gladders, Karl Glazebrook, Ben Jelliffe, Russell J. Jurek, I-hui Li, Barry Madore, D. Christopher Martin, Kevin Pimblet, Michael Pracy, Rob Sharp, Emily Wisnioski, David Woods, Ted K. Wyder, and H. K. C. Yee. The WiggleZ Dark Energy Survey: measuring the cosmic growth rate with the two-point galaxy correlation function. *Monthly Notices of the Royal Astronomical Society*, 430(2):924–933, February 2013.
- [22] S. de la Torre, L. Guzzo, J. A. Peacock, E. Branchini, A. Iovino, B. R. Granett, U. Abbas, C. Adami, S. Arnouts, J. Bel, M. Bolzonella, D. Bottini, A. Cappi, J. Coupon, O. Cucciati, I. Davidzon, G. De Lucia, A. Fritz, P. Franzetti, M. Fumana, B. Garilli, O. Ilbert, J. Krywult, V. Le Brun, O. Le Fèvre, D. Maccagni, K. Maek, F. Marulli, H. J. McCracken, L. Moscardini, L. Paioro, W. J. Percival, M. Polletta, A. Pollo, H. Schlegelhauser, M. Scodreggio, L. A. M. Tasca, R. Tojeiro, D. Vergani, A. Zanichelli, A. Burden, C. Di Porto, A. Marchetti, C. Marinoni, Y. Mellier, P. Monaco, R. C. Nichol, S. Phleps, M. Wolk, and G. Zamorani. The VI-MOS Public Extragalactic Redshift Survey (VIPERS). *Astronomy & Astrophysics*, 557:A54, August 2013.
- [23] Lado Samushia, Beth A Reid, Martin White, Will J Percival, Antonio J. Cuesta, Lucas Lombriser, Marc Manera, Robert C Nichol, Donald P. Schneider, Dmitry Bizyaev, Howard Brewington, E. Malanushenko, Viktor Malanushenko, Daniel Oravetz, Kaike Pan, Audrey Simmons, Alaina Shelden, Stephanie Snedden, Jeremy L Tinker, Benjamin A Weaver, Donald G York, and G.-B. Zhao. The clustering of galaxies in the SDSS-III DR9 Baryon Oscillation Spectroscopic Survey: testing deviations from and general relativity using anisotropic clustering of galaxies. *Monthly Notices of the Royal Astronomical Society*, 429(2):1514–1528, December 2012.
- [24] Beth A Reid, Lado Samushia, Martin White, Will J Percival, Marc Manera, Nikhil Padmanabhan, Ashley J. Ross, Ariel G. Sánchez, Stephen Bailey, Dmitry Bizyaev, Adam S Bolton, Howard Brewington, J Brinkmann, Joel R Brownstein, Antonio J Cuesta, Daniel J Eisenstein, James E Gunn, Klaus Honscheid, Elena Malanushenko, Viktor Malanushenko, Claudia Maraston, Cameron K. McBride, Demitri Muna, Robert C Nichol, Daniel Oravetz, Kaike Pan, Roland de Putter, N A Roe, Nicholas P Ross, David J Schlegel, Donald P Schneider, Hee-Jong Seo, Alaina Shelden, Erin S Sheldon, Audrey Simmons, Ramin A Skibba, Stephanie Snedden, Molly E C Swanson, Daniel Thomas, Jeremy Tinker, Rita Tojeiro, Licia Verde, David A Wake, Benjamin A Weaver, David H. Weinberg, Idit Zehavi, and Gong-Bo Zhao. The clustering

- of galaxies in the SDSS-III Baryon Oscillation Spectroscopic Survey: measurements of the growth of structure and expansion rate at $z = 0.57$ from anisotropic clustering. *Monthly Notices of the Royal Astronomical Society*, 426(4):2719–2737, November 2012.
- [25] Florian Beutler, Shun Saito, H.-J. Seo, Jon Brinkmann, Kyle S. Dawson, Daniel J Eisenstein, Andreu Font-Ribera, Shirley Ho, Cameron K. McBride, Francesco Montesano, Will J Percival, A. J. Ross, Nicholas P. Ross, Lado Samushia, David J Schlegel, A. G. Sanchez, Jeremy L. Tinker, and Benjamin A Weaver. The clustering of galaxies in the SDSS-III Baryon Oscillation Spectroscopic Survey: testing gravity with redshift space distortions using the power spectrum multipoles. *Monthly Notices of the Royal Astronomical Society*, 443(2):1065–1089, July 2014.
- [26] Akira Oka, Shun Saito, Takahiro Nishimichi, Atsushi Taruya, and Kazuhiro Yamamoto. Simultaneous constraints on the growth of structure and cosmic expansion from the multipole power spectra of the SDSS DR7 LRG sample. *Monthly Notices of the Royal Astronomical Society*, 439(3):2515–2530, February 2014.
- [27] R Bielby, M D Hill, T Shanks, N H M Crichton, L Infante, C G Bornancini, H Francke, P. Heraudeau, D G Lambas, N Metcalfe, D Minniti, N Padilla, T Theuns, P Tumuangpak, and P Weilbacher. The VLT LBG Redshift Survey - III. The clustering and dynamics of Lyman-break galaxies at $z \approx 3$. *Monthly Notices of the Royal Astronomical Society*, 430(1):425–449, January 2013.
- [28] Hiroyuki Okada, Tomonori Totani, and Shinji Tsujikawa. Constraints on $f(R)$ theory and Galileons from the latest data of galaxy redshift surveys. *Physical Review D*, 87(10):103002, May 2013.
- [29] Teppei Okumura and Y. P. Jing. SYSTEMATIC EFFECTS ON DETERMINATION OF THE GROWTH FACTOR FROM REDSHIFT-SPACE DISTORTIONS. *The Astrophysical Journal*, 726(1):5, January 2011.
- [30] K. B. Fisher, M. Davis, M. A. Strauss, A. Yahil, and J. P. Huchra. Clustering in the 1.2-Jy IRAS Galaxy Redshift Survey - II. Redshift distortions and Formula. *Monthly Notices of the Royal Astronomical Society*, 267(4):927–948, April 1994.
- [31] J. A. Peacock and S. J. Dodds. Reconstructing the linear power spectrum of cosmological mass fluctuations. *Monthly Notices of the Royal Astronomical Society*, 267(4):1020–1034, April 1994.
- [32] S. Hatton and S. Cole. Modelling the redshift-space distortion of galaxy clustering. *Monthly Notices of the Royal Astronomical Society*, 296(1):10–20, May 1998.
- [33] J. A. Peacock. *Cosmological Physics*. Cambridge University Press, Cambridge, 1998.
- [34] JL Tinker, DH Weinberg, and Zheng Zheng. Redshift - space distortions with the halo occupation distribution I. Numerical simulations. *Monthly Notices of the Royal Astronomical Society*, 368(1):85–108, 2006.
- [35] Román Scoccimarro. Redshift-space distortions, pairwise velocities, and nonlinearities. *Physical Review D*, 70(8):083007, October 2004.
- [36] Davide Bianchi, Luigi Guzzo, Enzo Branchini, Elisabetta Majerotto, Sylvain de la Torre, Federico Marulli, Lauro Moscardini, and Raul E. Angulo. Statistical and systematic errors in redshift-space distortion measurements from large surveys. *Monthly Notices of the Royal Astronomical Society*, 427(3):2420–2436, December 2012.
- [37] Atsushi Taruya, Takahiro Nishimichi, and Shun Saito. Baryon acoustic oscillations in 2D: Modeling redshift-space power spectrum from perturbation theory. *Physical Review D*, 82(6):063522, September 2010.
- [38] Takahiro Nishimichi and Atsushi Taruya. Baryon Acoustic Oscillations in 2D

- II: Redshift-space halo clustering in N-body simulations. *Physical Review D*, 84(4):043526, June 2011.
- [39] Jiayu Tang, Issha Kayo, and Masahiro Takada. Likelihood reconstruction method of real-space density and velocity power spectra from a redshift galaxy survey. *Monthly Notices of the Royal Astronomical Society*, 416(3):2291–2310, September 2011.
- [40] Uroš Seljak and Patrick McDonald. Distribution function approach to redshift space distortions. *Journal of Cosmology and Astroparticle Physics*, 2011(11):039–039, November 2011.
- [41] Beth A. Reid and Martin White. Towards an accurate model of the redshift-space clustering of haloes in the quasi-linear regime. *Monthly Notices of the Royal Astronomical Society*, 417(3):1913–1927, November 2011.
- [42] Juliana Kwan, Geraint F. Lewis, and Eric V Linder. MAPPING GROWTH AND GRAVITY WITH ROBUST REDSHIFT SPACE DISTORTIONS. *The Astrophysical Journal*, 748(2):78, April 2012.
- [43] Sylvain de la Torre and Luigi Guzzo. Modelling non-linear redshift-space distortions in the galaxy clustering pattern: systematic errors on the growth rate parameter. *Monthly Notices of the Royal Astronomical Society*, 427(1):327–342, November 2012.
- [44] E. Jennings, C. M. Baugh, and S. Pascoli. TESTING GRAVITY USING THE GROWTH OF LARGE-SCALE STRUCTURE IN THE UNIVERSE. *The Astrophysical Journal*, 727(1):L9, January 2011.
- [45] E Jennings, C. M. Baugh, and S Pascoli. Modelling redshift space distortions in hierarchical cosmologies. *Monthly Notices of the Royal Astronomical Society*, 410:2081–2094, 2011.
- [46] C. Contreras, C. Blake, G. B. Poole, and F. Marin. Determining accurate measurements of the growth rate from the galaxy correlation function in simulations. *Monthly Notices of the Royal Astronomical Society*, 430(2):934–945, January 2013.
- [47] E. Komatsu, K. M. Smith, J. Dunkley, C. L. Bennett, B. Gold, G. Hinshaw, N. Jarosik, D. Larson, M. R. Nolta, L. Page, D. N. Spergel, M. Halpern, R. S. Hill, A. Kogut, M. Limon, S. S. Meyer, N. Odegard, G. S. Tucker, J. L. Weiland, E. Wollack, and E. L. Wright. SEVEN-YEAR WILKINSON MICROWAVE ANISOTROPY PROBE (WMAP) OBSERVATIONS: COSMOLOGICAL INTERPRETATION. *The Astrophysical Journal Supplement Series*, 192(2):18, February 2011.
- [48] Antony Lewis, Anthony Challinor, and Anthony Lasenby. Efficient Computation of Cosmic Microwave Background Anisotropies in Closed Friedmann - Robertson - Walker Models. *The Astrophysical Journal*, 538(2):473–476, August 2000.
- [49] Will J. Percival and Martin White. Testing cosmological structure formation using redshift-space distortions. *Monthly Notices of the Royal Astronomical Society*, 393(1):297–308, February 2009.
- [50] M. Davis, G. Efstathiou, C. S. Frenk, and S. D. M. White. The evolution of large-scale structure in a universe dominated by cold dark matter. *The Astrophysical Journal*, 292:371, May 1985.
- [51] N. Kaiser. On the spatial correlations of Abell clusters. *The Astrophysical Journal*, 284:L9, September 1984.
- [52] Volker Springel, Naoki Yoshida, and Simon D.M. White. GADGET: a code for collisionless and gasdynamical cosmological simulations. *New Astronomy*, 6(2):79–117, April 2001.
- [53] V. Springel. The cosmological simulation code GADGET-2. *Monthly Notices of the*

- Royal Astronomical Society*, 364(4):1105–1134, December 2005.
- [54] T. Ishikawa, T. Totani, T. Nishimichi, R. Takahashi, N. Yoshida, and M. Tonegawa. On the systematic errors of cosmological-scale gravity tests using redshift-space distortion: non-linear effects and the halo bias. *Monthly Notices of the Royal Astronomical Society*, 443(4):3359–3367, August 2014.
- [55] Takahiro Nishimichi, Akihito Shirata, Atsushi Taruya, Kazuhiro Yahata, Shun Saito, Yasushi Suto, Ryuichi Takahashi, Naoki Yoshida, Takahiko Matsubara, Naoshi Sugiyama, Issha Kayo, Yipeng Jing, and Kohji Yoshikawa. Modeling Nonlinear Evolution of Baryon Acoustic Oscillations: Convergence Regime of n -body Simulations and Analytic Models. *Publications of the Astronomical Society of Japan*, 61(2):321–332, April 2009.
- [56] P Valageas and T Nishimichi. Combining perturbation theories with halo models for the matter bispectrum. *Astronomy & Astrophysics*, 532:A4, July 2011.
- [57] Volker Springel, Simon D. M. White, Giuseppe Tormen, and Guinevere Kauffmann. Populating a cluster of galaxies - I. Results at $z=0$. *Monthly Notices of the Royal Astronomical Society*, 328(3):726–750, December 2001.
- [58] Takahiro Nishimichi and Akira Oka. Simulating the anisotropic clustering of luminous red galaxies with subhaloes: a direct confrontation with observation and cosmological implications. *Monthly Notices of the Royal Astronomical Society*, 444(2):1400–1418, August 2014.
- [59] R W Hockney and J W Eastwood. *Computer Simulation Using Particles*. IOP Publishing Ltd, 1988.
- [60] Ryuichi Takahashi, Naoki Yoshida, Takahiko Matsubara, Naoshi Sugiyama, Issha Kayo, Takahiro Nishimichi, Akihito Shirata, Atsushi Taruya, Shun Saito, Kazuhiro Yahata, and Yasushi Suto. Simulations of Baryon Acoustic Oscillations I: Growth of Large-Scale Density Fluctuations. *Monthly Notices of the Royal Astronomical Society*, 389(4):1675–1682, 2008.
- [61] Ryuichi Takahashi, Naoki Yoshida, Masahiro Takada, Takahiko Matsubara, Naoshi Sugiyama, Issha Kayo, Atsushi J. Nishizawa, Takahiro Nishimichi, Shun Saito, and Atsushi Taruya. SIMULATIONS OF BARYON ACOUSTIC OSCILLATIONS. II. COVARIANCE MATRIX OF THE MATTER POWER SPECTRUM. *The Astrophysical Journal*, 700(1):479–490, July 2009.
- [62] Hume A. Feldman, Nick Kaiser, and John A. Peacock. Power-spectrum analysis of three-dimensional redshift surveys. *The Astrophysical Journal*, 426:23, May 1994.
- [63] Atsushi Taruya and Takashi Hiramatsu. A Closure Theory for Nonlinear Evolution of Cosmological Power Spectra. *The Astrophysical Journal*, 674(2):617–635, February 2008.
- [64] Atsushi Taruya, Takahiro Nishimichi, Shun Saito, and Takashi Hiramatsu. Nonlinear evolution of baryon acoustic oscillations from improved perturbation theory in real and redshift spaces. *Physical Review D*, 80(12):123503, December 2009.
- [65] Andrew Gelman and Donald B. Rubin. Inference from Iterative Simulation Using Multiple Sequences. *Statistical Science*, 7(4):457–472, November 1992.
- [66] Shaun Cole, Karl B. Fisher, and David H. Weinberg. Fourier analysis of redshift-space distortions and the determination of. *Monthly Notices of the Royal Astronomical Society*, 267(3):785–799, April 1994.
- [67] E. B. Wilson and M. M. Hilferty. The Distribution of Chi-Square. *Proceedings of the National Academy of Sciences*, 17(12):684–688, December 1931.
- [68] Ravi K Sheth and Giuseppe Tormen. Large-scale bias and the peak background split.

- Monthly Notices of the Royal Astronomical Society*, 308(1):119–126, September 1999.
- [69] Yong-seon Song and Will J Percival. Reconstructing the history of structure formation using redshift distortions. *Journal of Cosmology and Astroparticle Physics*, 2009(10):004–004, October 2009.